

Turbulence statistics and structures of drag-reducing turbulent boundary layer in homogeneous aqueous surfactant solutions

Shinji Tamano,^{1,a)} Motoyuki Itoh,¹ Takefumi Inoue,² Katsuo Kato,¹ and Kazuhiko Yokota¹

¹Graduate School of Engineering, Nagoya Institute of Technology, Gokiso-cho, Showa-ku, Nagoya, Aichi 466-8555, Japan

²Kawasaki Heavy Industries, 1-1, Kawasaki-cho, Akashi, Hyogo 673-8666, Japan

(Received 23 May 2008; accepted 10 February 2009; published online 8 April 2009)

In our earlier work [Itoh *et al.*, Phys. Fluids **17**, 075107 (2005)], the additional maximum of the streamwise turbulence intensity near the center of the drag-reducing turbulent boundary layer was found in the homogeneous dilute aqueous surfactant solution which was a mixture of cetyltrimethyl ammonium chloride with sodium salicylate as counterion. In this work, we systematically investigated the influence of the drag-reducing surfactant on the velocity fields of the turbulent boundary layer at various Reynolds numbers Re_θ from 301 to 1437 and the drag reduction ratio DR from 8% to 74% under different streamwise locations and concentration and temperature of solutions using a two-component laser-Doppler velocimetry (LDV) system. It was revealed that all data on DR versus the wall-shear rate obtained here were collapsed on a single curve. We verified the existence of the additional maximum of the streamwise turbulence intensity near the center of the boundary layer which appeared at relatively large drag reduction ratios and small Reynolds numbers. It was found that the additional maximum of streamwise turbulence intensity and its wall-normal location were independent of the streamwise location, wall-shear rate, Reynolds number, and drag reduction ratio. The additional maximum could be explained by the bilayered structure model proposed, in which the flow in the near-wall region is in shear-induced structure (SIS) and viscoelastic, whereas the flow in the region away from the wall is in non-SIS and nonviscoelastic. This model was based on measurements of the shear viscosity. We also performed particle image velocimetry measurements, which revealed that the fluctuating velocity vector fields showed two situations, with low and high activity. In low activity, the velocity fluctuations were attenuated largely across the turbulent boundary layer. In high activity, fluctuating velocity vectors were almost parallel to the wall and relatively large in both regions near the wall and the center of the boundary layer, which seemed to be a bilayered structure and supported the bilayered structure model. © 2009 American Institute of Physics. [DOI: 10.1063/1.3103884]

I. INTRODUCTION

It is well known that a drag reduction in up to 80% can be achieved by the addition of a small amount of a surfactant or polymer to a wall-bounded turbulent flow.^{1–3} Surfactant additives are attractive as practical drag-reducing additives because they are not affected by the degradation due to mechanical shear action and they could apply to the circulatory system. Recently, velocity measurements of a drag-reducing turbulent channel and pipe flows of surfactant solutions have yielded valuable knowledge about the suppression of turbulence, the modification of quasistreamwise vortices, hairpin vortices, and low-speed streaks, and the stress deficit in which the sum of viscous and turbulent shear stresses is not equal to the total shear stress.^{4–14} On the other hand, there have been few experimental studies on the drag-reducing effect of viscoelastic fluids such as polymer and surfactant solutions for a turbulent boundary layer, which is a typical external flow.

Koskie and Tiederman,^{15,16} Fontaine *et al.*,¹⁷ and Petrie *et al.*¹⁸ investigated the drag reduction by injection of polymer solutions for a turbulent boundary layer using laser-Doppler velocimetry (LDV) measurements. Recently, White *et al.*¹⁹ and Hou *et al.*^{20,21} clarified the effects of polymer additives on the turbulent boundary layer using the particle image velocimetry (PIV) measurements. A quite recent review of the drag reduction of turbulent boundary layer due to the injection of polymer was reported by White and Mungal²² and Hou *et al.*²¹ Regarding the drag reduction in the turbulent boundary layer due to surfactant additives, Itoh *et al.*²³ found that the streamwise turbulence intensity had a maximum near the center of the turbulent boundary layer in addition to the near-wall maximum which appears in canonical wall-bounded turbulent flow using LDV measurements. However, their LDV measurements were conducted for only one experimental condition of the combination of solution concentration and temperature. There are not enough data to prove the existence of the additional maximum owing to the lack of the appropriate experimental conditions. In addition, turbulence structures, of which data are helpful for understanding the mechanism of the drag reduction, have not been sufficiently studied for the drag-reducing turbulent boundary

^{a)}Author to whom correspondence should be addressed. Telephone: +81-52-735-5609. Fax: +81-52-735-5247. Electronic mail: tamano.shinji@nitech.ac.jp.

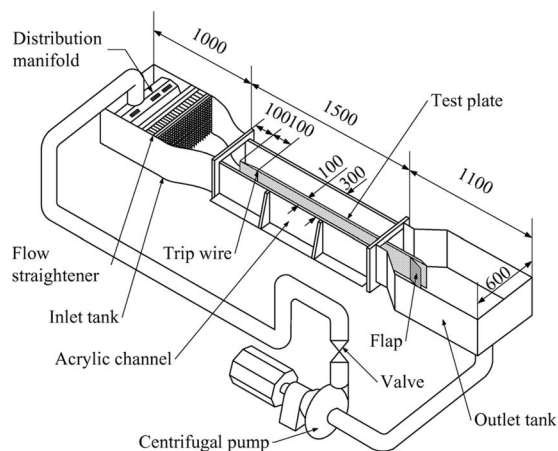


FIG. 1. Experimental apparatus.

layer of surfactant solutions.²² Therefore, the present study represents a significant extension in this regard.

Recently, Dimitropoulos *et al.*^{24,25} performed a direct numerical simulation (DNS) of a polymer-induced drag-reducing zero-pressure gradient turbulent boundary layer flow using the FENE-P model. Their DNS can predict some experimental measurements of White *et al.*¹⁹ on a developing boundary layer in polymer solutions. Tamano *et al.*²⁶ also reported the DNS results of drag-reducing turbulent boundary layer in viscoelastic fluids using the Oldroyd-B and Giesekus models. However, these previous DNSs have not dealt with the drag-reducing turbulent boundary layer of surfactant solutions, and could not predict the velocity fields with the additional maximum of the streamwise turbulence intensity observed in our previous experiments.

In the present study, the mean velocity and turbulence statistics in a zero-pressure gradient turbulent boundary layer of a homogeneous drag-reducing surfactant [cetyltrimethyl ammonium chloride (CTAC)] solution were systematically measured at various Reynolds numbers using a two-component LDV system under a different solution concentration and temperature. In addition, the turbulence structures were investigated by the PIV measurements. The present experimental data which were not obtained in previous study can be valuable and helpful for constructing the new constitutive equation models for the DNS which capture the new physics of drag reduction of a turbulent boundary layer in dilute aqueous surfactant solutions.²⁶

II. EXPERIMENTAL APPARATUS AND PROCEDURE

The experiments were conducted in a closed-loop water tunnel with a cross section of $300 \times 300 \text{ mm}^2$ and a length of 1500 mm in which a test plate of $20 \times 295 \times 1700 \text{ mm}^3$ was installed, where the test plate was perpendicular to the bottom surface of the acrylic channel (see Fig. 1). All parts in contact with the surfactant solution were made of acrylic resin or stainless steel. For the LDV measurement in Sec. III, a 2 mm diameter trip wire was fixed 100 mm downstream from the leading edge to assure a consistent transition location. We also used 1 mm diameter trip wire for the LDV and PIV measurements in Sec. IV, and confirmed that the influ-

ence of the trip wire diameter on flow fields was negligible in the present study. The difference in free-stream velocities ($U_e \approx 300 \text{ mm/s}$) between the location of the leading edge of the test plate and the location 1000 mm downstream was less than 1%, where the flap was used for the zero-pressure gradient turbulent boundary layer. The working fluids were circulated by a stainless steel centrifugal pump. The turbulence and spatial irregularities of the flow were reduced by passing through porous plates, honeycombs, and mesh screens. After that, the flow was made uniform by a convergent nozzle. We also confirmed that the free-stream turbulence intensity was less than 2%.

The surfactant solution used here was a mixture of cetyltrimethyl ammonium chloride (C_{16}TACl , CTAC) with sodium salicylate (NaSal) as counterion, which was dissolved in tap water. We confirmed that the difference in velocity profile using tap water and de-ionized water was negligible. The concentrations of surfactant (CTAC) C tested were 65, 100, and 150 ppm by weight. Here, the $C=65$ ppm for the surfactant solution (CTAC) corresponds to the 75 ppm for the surfactant solution ($\text{C}_{16}\text{TASal}$) in our previous study.²³ The molar ratio of counterion to CTAC was one, and the solution temperature T was 20, 25, 30, and 35 °C. The surfactant solutions tested were gently stirred for several hours in a head tank before pouring into the water tunnel. The concentration of surfactant solution in the boundary layer flow was homogeneous.

The shear viscosity η of the surfactant solutions tested was measured using a homemade capillary viscometer, in which the gravity flow was generated by the head tank of 1000 mm. The stainless smooth pipe with an internal diameter of $d=5.07 \text{ mm}$ was used. The flow rate was controlled by the needle valve and measured in terms of the weighing method. The developing region is 600 mm long ($=120d$), and the measuring region is 1400 mm long ($=280d$), which indicates that the shear viscosity of presheared surfactant solutions can be obtained. On the other hand, for the turbulent boundary layer flow, the shear-induced structure (SIS) (see below for details) is not formed just upstream of the test section, since the SIS is destroyed due to the large wall-shear stress in the pump and pipe flows upstream of the inlet tank. A pressure transducer (GE Druck Co., Ltd., LPM5481) with a full scale of 200 Pa and linearity of $\pm 0.25\%$ was used for measurements of pressure loss in the measuring region. The water-jacketed structure kept solution temperature variation within $\pm 0.5 \text{ }^\circ\text{C}$ during shear viscosity measurement. Here, the shear viscosity could not be measured by using the rheometer correctly, because the surfactant solutions used were very dilute.

Figure 2(a) shows that the shear viscosity η at temperature $T=20 \text{ }^\circ\text{C}$ for $C=65, 100,$ and 150 ppm . It is observed that the η increases with the increase in C . For all the concentrations at $T=20 \text{ }^\circ\text{C}$, the η suddenly increased around the shear rate $\dot{\gamma}_w=10 \text{ 1/s}$. This phenomenon is called the shear-induced state or structure (SIS).^{2,3,27,28} At the low shear rate ($\dot{\gamma}_w \approx 10 \text{ 1/s}$), the experimental uncertainty in η was estimated to be $\pm 10\%$ of its absolute value, which was too large to accurately identify the shear rate of the onset of SIS. Shear thinning can also be observed where the η decreases gradu-

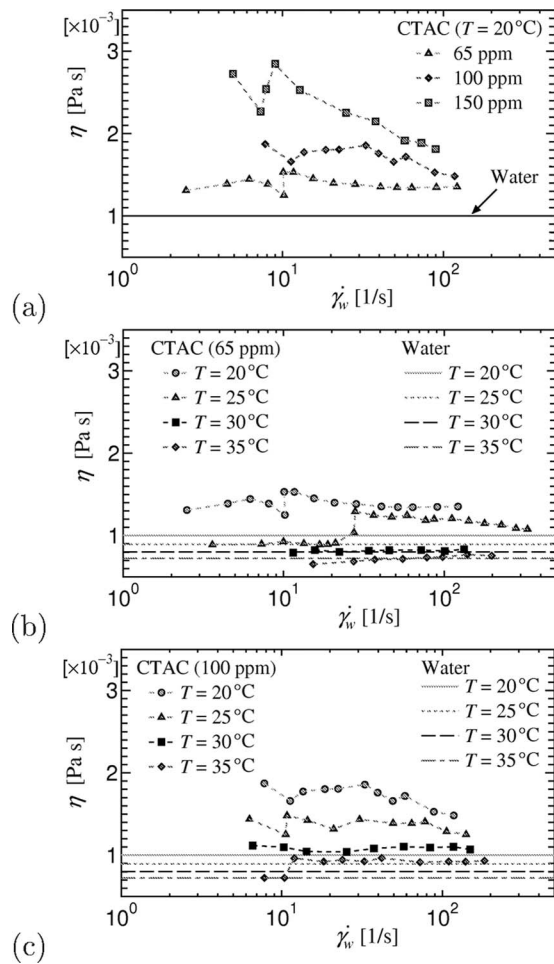


FIG. 2. Shear viscosity: (a) $T=20^\circ\text{C}$, (b) $C=65$ ppm, and (c) $C=100$ ppm.

ally with an increase in $\dot{\gamma}_w$. The magnitude of the shear thinning for $C=150$ ppm is much larger than that for $C=65$ and 100 ppm. Figures 2(b) and 2(c) show the η at $T=20, 25, 30,$ and 35°C for $C=65$ and 100 ppm, respectively. It is evident that the η for both $C=65$ and 100 ppm decreases with the increase in T . For $C=65$ ppm, the SIS is observed at $\dot{\gamma}_w \approx 10$ 1/s and 20 1/s at $T=20$ and 25°C , respectively, not at $T=30$ and 35°C . For $C=65$ ppm, the shear thinning is observed at $T=20$ and 25°C , not at $T=30$ and 35°C . Figure 2(c) shows that the SIS for $C=100$ ppm is observed at $\dot{\gamma}_w \approx 10$ 1/s at $T=20, 25,$ and 35°C , not at $T=30$ and 35°C . Although the data on η for $C=100$ ppm seem to be slightly scattered, the shear thinning is observed at $T=20$ and 25°C , not at $T=30$ and 35°C .

In order to clarify the order of the critical wall-shear stress of drag-reducing surfactant solutions used here at which the SIS is destroyed, we also investigated the relation of the friction factor and the Reynolds number for the pipe flow with the internal diameter of $d=5.07$ mm. The pressurized flow rate was generated by the pressure tank operated at high pressure up to 0.5 MPa. The developing region is 700 mm long ($=140d$), and the measuring region is 70 mm long ($=14d$). The pressure transducer (GE Druck Co., Ltd., LPM5481) whose full scale was 20 000 Pa and linearity was $\pm 0.25\%$ was used for measurements of pressure loss. The

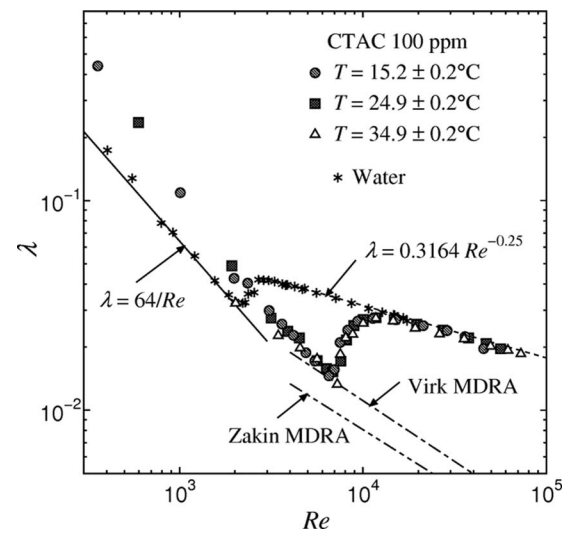


FIG. 3. Friction factor vs Reynolds number in pipe flow for CTAC of 100 ppm.

temperature variation was within $\pm 0.2^\circ\text{C}$ during measurement. Figure 3 shows the relation between the friction factor λ and the Reynolds number Re at $T \approx 15, 25,$ and 35°C for CTAC 100 ppm. The Reynolds number $Re = U_m d / \nu_w$ is based on the bulk velocity U_m and the kinematic viscosity of water ν_w . This figure also presents the Hagen–Poiseuille laminar theoretical relation ($\lambda = 64/Re$) and the Blasius turbulent empirical relation ($\lambda = 0.3164 Re^{-0.25}$) for Newtonian fluid, Virk's maximum drag reduction asymptote (MDRA) for polymer solutions¹ ($\lambda = 2.32 Re^{-0.58}$, $4000 < Re < 40\,000$), and Zakin's MDRA for surfactant solutions³ ($\lambda = 1.28 Re^{-0.55}$). The relation between λ and Re seems to be independent of the solution temperature, in which the maximum drag reduction ratio was about 60%. It is found that the drag-reducing effect of surfactant solutions suddenly disappears beyond a critical Reynolds number, i.e., a critical wall-shear stress, unlike the dilute polymer solutions. For CTAC 100 ppm, the critical wall-shear stresses at $T \approx 15, 25,$ and 35°C were 4.0, 2.9, and 1.8 Pa, respectively. For both $C=65$ and 150 ppm, the order of the critical wall-shear stress was also $O(10^0)$ Pa. Note that the critical wall-shear stress is independent of the diameter of the pipe for the surfactant solution.³

For the turbulent boundary layer experiment, the two-component LDV system (300 mW argon-ion laser) was used in back scatter mode. The laser light was separated into green and blue beams with wavelengths of 514.5 and 488.0 nm, respectively, and then passed through the bottom of the channel. The measuring volumes are 0.072×0.864 mm² for the green beams and 0.068×0.824 mm² for the blue beams. The shift frequencies for blue and green beams were set at 200 kHz. The probe was slightly tilted (3°) with respect to the test plate surface in order to measure velocity very close to the wall. The velocity data were taken at angles of $\pm 45^\circ$ to the main flow direction in order to measure the Reynolds shear stress. The flow was seeded with nylon powder particles (mean diameter: 4.1 μm and specific gravity: 1.02). The particle concentration was about 5 ppm for the LDV

TABLE I. Boundary layer parameters and friction velocity for $C=65, 100, 150$ ppm at $T=20$ °C and water at $T=25$ °C.

	x (mm)	δ (mm)	δ^* (mm)	θ (mm)	u_τ (mm/s)
CTAC 65 ppm	300	12.7	2.91	1.63	13.2
	500	16.8	3.71	2.04	10.6
	800	20.5	4.50	2.47	9.50
	1000	23.0	4.87	2.65	8.50
CTAC 100 ppm	300	14.5	3.29	1.89	13.9
	500	15.5	3.82	2.05	11.4
	800	21.0	5.21	2.84	10.1
	1000	22.2	5.45	2.90	9.60
CTAC 150 ppm	300	13.4	3.03	1.72	14.2
	500	15.7	3.71	2.04	13.0
	800	19.6	4.70	2.60	11.8
	1000	21.5	5.38	2.96	11.2
Water	300	15.1	2.76	1.89	14.8
	500	20.7	3.51	2.41	14.4
	800	26.3	4.28	3.00	14.1
	1000	29.5	4.91	3.43	13.8

measurement. The residual air was removed by running the water tunnel for several hours before the velocity measurements. LDV measurements under free-stream velocity $U_e \approx 300$ mm/s were made 150 mm height above the channel bottom, and at locations downstream from the leading edge where $x=300, 500, 800,$ or 1000 mm. A refrigerator controlled the variation of solution temperature within ± 0.1 °C during LDV measurements. Typical data rates in the locations away from the wall were about 200 Hz, falling off to about 40 Hz very close to the wall. Data samples in the locations away from and near the wall were about 25 000 and 10 000, respectively.

The two-dimensional PIV measurement was conducted for the section normal to the test plate (the streamwise and wall-normal section) which was illuminated by a laser sheet (LYPE-2SG-WL532CW, output: 1.5 W, width: 2 mm, Japan Laser, Ltd.) through the side wall of the channel, and images were captured by a high-speed camera (FASTCAM-1024PCI, Photron, Ltd.) from the bottom of the channel. The high-speed camera has a resolution of 1024×1024 pixels. The frame rate was set at 500 frames/s. The shutter speed was $1/5000$ s. The flow was seeded with particles (Orgasol, mean diameter: $50 \mu\text{m}$; specific gravity: 1.02). The particle concentrations for PIV measurements were about 70 and 50 ppm for water and surfactant solutions, respectively. In the present study, we used the original PIV program based on the direct correlation method to obtain the velocity vector field. The interrogation region was 70×40 pixels with 57% and 75% overlap in the streamwise and wall-normal direction, respectively. The search region was 40×20 pixels. The spatial resolution of the camera was $39 \mu\text{m}/\text{pixel}$ with an effective field of view of $40 \times 40 \text{ mm}^2$. PIV measurements were made for the water and the surfactant

TABLE II. Boundary layer parameters and friction velocity at $x=1000$ mm for $C=65$ and 100 ppm.

	T (°C)	δ (mm)	δ^* (mm)	θ (mm)	u_τ (mm/s)
CTAC 65 ppm	20	23.0	4.87	2.65	8.50
	25	22.2	5.13	2.58	7.70
	30	28.1	4.69	3.25	11.3
	35	29.8	4.79	3.43	13.0
CTAC 100 ppm	20	22.2	5.45	2.90	9.60
	25	20.1	4.89	2.52	8.50
	30	24.3	4.74	2.75	10.5
	35	29.3	4.60	3.21	12.5

solution $C=100$ ppm at the location of 1000 mm downstream from the leading edge under the free-stream velocity $U_e \approx 300$ mm/s and the solution temperature $T=20 \pm 0.1$ °C. The turbulent statistics were obtained by evaluating 3000 images in PIV vector fields. Erroneous velocity vectors were removed, and the missing data were supplemented by interpolation of neighboring velocity vectors. The fluctuating velocity vector fields were obtained by the Reynolds decomposition.

III. LDV MEASUREMENTS

A. Boundary layer parameters

Table I shows the comprehensive listing of the boundary layer parameters such as the boundary layer thickness δ , displacement thickness δ^* , momentum thickness θ , and the friction velocity u_τ at $x=300, 500, 800,$ and 1000 mm for the surfactant solutions of $C=65, 100,$ and 150 ppm at $T=20$ °C and water at $T=25$ °C. The data on $C=65$ ppm and $T=20$ °C are the same as those of our previous study.²³ The friction velocity u_τ was obtained by estimating the wall-shear stress from the mean velocity gradient and the shear viscosity at the wall for the surfactant solution, and by the Clauser method for water. The uncertainty in u_τ was estimated at $\pm 3\%$ of its absolute value. Table I shows that the length scales δ and θ for the surfactant solutions for all the concentrations are smaller than those for water at the same streamwise location x , respectively. The length scale δ^* for the surfactant solutions is not so different from that for water at the corresponding streamwise location. The u_τ for the surfactant solutions is smaller than that for water at the same x , which means the drag reduction (see Table III in detail). Table II shows the $\delta, \delta^*, \theta,$ and u_τ at $T=20, 25, 30,$ and

TABLE III. Drag reduction ratio DR (%) at $T=20$ °C for $C=65, 100,$ and 150 ppm.

C (ppm)	$x=300$ (mm)	$x=500$ (mm)	$x=800$ (mm)	$x=1000$ (mm)
65	36	56	63	69
100	34	53	58	63
150	31	42	49	50

TABLE IV. Drag reduction ratio DR (%) at $x=1000$ mm for $C=65$ and 100 ppm.

C (ppm)	$T=20$ °C	$T=25$ °C	$T=30$ °C	$T=35$ °C
65	69	74	33	8
100	63	70	49	20

35 °C, and $x=1000$ mm for $C=65$ and 100 ppm. For both $C=65$ and 100 ppm, the values of δ , θ , and u_τ decrease from $T=20$ to 25 °C, and increase from $T=25$ to 35 °C. The dependence of δ , θ , and u_τ on temperature for both $C=65$ and 100 ppm corresponds to that of the drag reduction ratio (see Table IV), while the development of δ^* does not.

Figures 4(a) and 4(b) show the dependence of the friction coefficient $C_f=2(u_\tau/U_e)^2$ on the streamwise location x and the momentum-thickness Reynolds number $Re_\theta=U_e\theta/\nu$ at $x=300, 500, 800,$ and 1000 mm and $T=20$ °C for $C=65, 100,$ and 150 ppm, respectively. The kinematic viscosity ν for surfactant solution was determined using the shear rate at the wall. In Fig. 4(b), the solid and dotted lines represent Coles' curve²⁹ and Blasius laminar line,³⁰ respectively. Figure 4(a) shows that the C_f monotonically decreases in the streamwise direction, in which the slope becomes larger with the decrease in solution concentration. On the other hand, it is noticeable that the data of C_f versus the Reynolds number Re_θ are collapsed for all the concentrations of surfactant solutions at $T=20$ °C [Fig. 4(b)], in which the values of C_f drastically decrease with the increase in Re_θ , and the difference between surfactant solution and water becomes larger. Figure 5 shows the dependence of the $C_f=2(u_\tau/U_e)^2$ on the Re_θ at $T=20, 25, 30,$ and 35 °C and $x=1000$ mm for

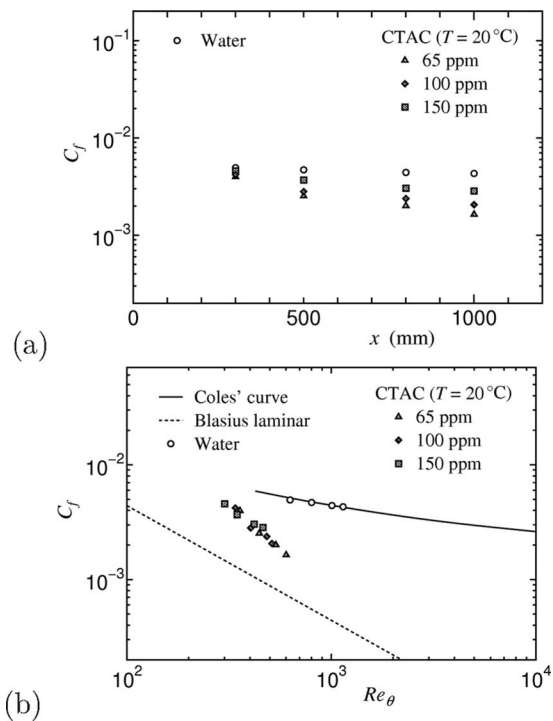


FIG. 4. Friction coefficient: (a) vs x mm and (b) vs Re_θ .

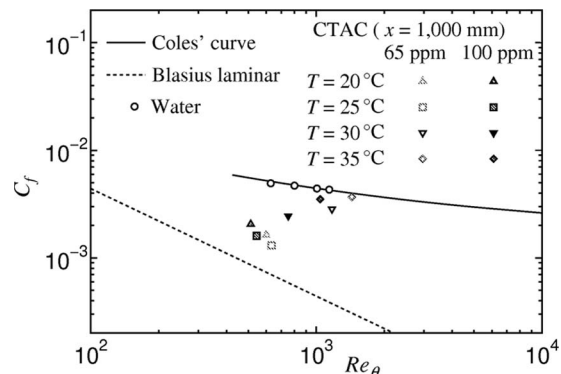


FIG. 5. Friction coefficient vs Reynolds number.

$C=65$ and 100 ppm. The values of C_f for both $C=65$ and 100 ppm are smallest at $T=25$ °C ($Re_\theta \approx 600$). With the increase in T from 25 to 35 °C, i.e., from $Re_\theta \approx 600$ to 1400, the C_f approaches Coles' curve.

Figures 6(a) and 6(b) show the dependence of the shape factor $H=\delta^*/\theta$ on x and Re_θ at $x=300, 500, 800,$ and 1000 mm and $T=20$ °C for $C=65, 100,$ and 150 ppm, respectively. The values of H for the surfactant solution at $T=20$ °C are much larger than those for water, ranging between the value for the laminar flow ($H=2.59$) and those for the turbulent flow of Newtonian fluid. These trends are independent of both x and Re_θ . For all the solution concentration at $T=20$ °C, the value of H slightly increases with the increase in x or Re_θ , while it decreases for water. Figure 7 shows the dependence of the H on Re_θ at $T=20, 25, 30,$ and 35 °C and $x=1000$ mm for $C=65$ and 100 ppm. The values of H for both $C=65$ and 100 ppm increase from $T=20$

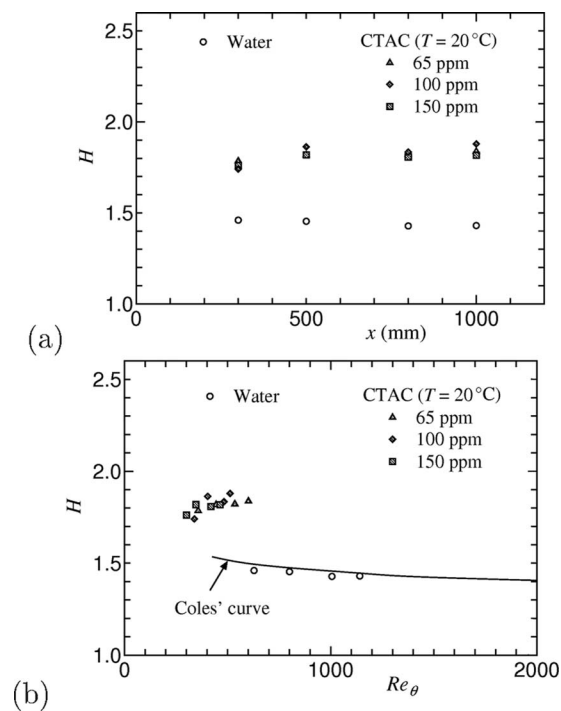


FIG. 6. Shape factor: (a) vs x mm and (b) vs Re_θ .

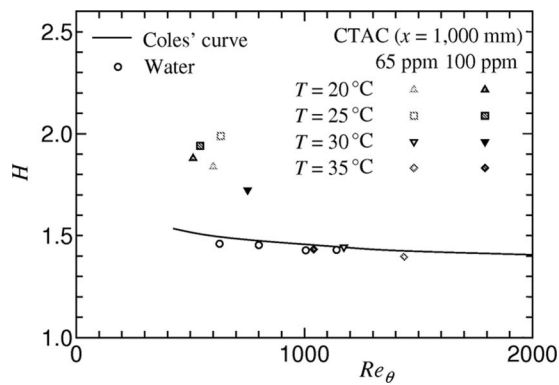


FIG. 7. Shape factor vs Reynolds number.

25 °C, and then approach Coles' curve from $T=25$ to 35 °C, i.e., from $Re_\theta \approx 600$ to 1400, whose variation corresponds to that of C_f (see Fig. 5).

B. Drag reduction ratio

In the present study, the drag reduction ratio DR is defined as follows:

$$DR = \frac{C_{f,\text{water}} - C_{f,\text{surfactant}}}{C_{f,\text{water}}} \times 100, \quad (1)$$

under the condition of the same momentum-thickness Reynolds number Re_θ . The C_f for water is obtained using Coles' curve at the corresponding Reynolds number. Note that the condition for the evaluation of DR is different from that of our previous study,²³ in which the DR is obtained at the same streamwise position and free-stream velocity. The uncertainty in DR was estimated at $\pm 5\%$ of its absolute value. Table III shows the DR at $x=300, 500, 800,$ and 1000 mm and $T=20$ °C for $C=65, 100,$ and 150 ppm, while Table IV shows the DR at $T=20, 25, 30,$ and 35 °C and $x=1000$ mm for $C=65$ and 100 ppm. The DR becomes larger downstream from $x=300$ to 1000 mm, and decreases with the increase in concentration from $C=65$ to 150 ppm (Table III). The DR for both $C=65$ and 100 ppm becomes smaller with the increase in temperature from $T=25$ to 35 °C, and the DR at $T=20$ °C is smaller than the DR at $T=25$ °C (Table IV). In the present study, the maximum drag reduction ratio DR defined at the same momentum-thickness Reynolds number is $DR=74\%$ at $T=25$ °C and $x=1000$ mm for $C=65$ ppm, which corresponds to the 69% of the drag reduction ratio DR defined at the same streamwise and free-stream velocity.

With flow of the homogeneous surfactant solution at a constant temperature, the streamwise variation in DR is due to a downstream modification of solution properties. For the pipe flow of polymer solutions, Kulik³¹ reported three regions with different streamwise modifications of DR: growth, maximum, and slope down. These regions seem to be also apparent in the present study as follows. In the growth region, the DR at $T=20$ °C increases along the whole plate. It is deduced that the $DR=74\%$, which is obtained at $T=25$ °C and $x=1000$ mm for $C=65$ ppm, is in the maximum region without showing the data at

$x > 1000$ mm. The DR appears to decrease with the increase in T in the slope down region. However, this plausible explanation in the slope down region is not applicable to the present study on turbulent boundary layer flow in surfactant solutions under different concentration and temperature of solutions (see below for details).

Regarding the drag-reducing effect of surfactant solution, Li *et al.*¹² categorized the turbulent channel flow of the CTAC solution into four regimes, based on the relationship between the Reynolds number and the drag reduction levels. Yu and Kawaguchi³² also proposed a bilayer model to explain their experimental results¹² in channel flows of surfactant solutions, in which the drag reduction ratio DR was a nonmonotonic function of the Reynolds number. At the subcritical Reynolds number (before the peak value of DR was reached), network structures of rodlike micelles (SIS) were formed near the wall and were absent in the center of the channel, whereas at the supercritical Reynolds number (after DR passed the peak value) the shear rate near the channel center was large enough to form SIS, while near the wall the shear rate was so large that SIS was mostly broken. Therefore, qualitatively different turbulence statistics profiles were observed for subcritical and supercritical Reynolds number flows even though their DR might be very close to one another.¹²

In the present study, the variation in DR with Re_θ seems to correspond to that for the turbulent channel flow¹² [see Fig. 8(a)]. However, the complex process of formation and reversible destruction of network structures of rodlike micelles in the solution cannot be described only by a single parameter Re_θ . The reason why the DR versus Re_θ seems to be almost collapsed may be due to that all velocity measurements are performed only at a single free-stream velocity. Since the formation and destruction of SIS are more closely related to the wall-shear rate or the wall-shear stress, rather than to the Reynolds number, we should consider the drag reduction ratio DR versus the wall-shear rate $\dot{\gamma}_w$ and the wall-shear stress τ_w which are shown in Figs. 8(b) and 8(c), respectively. The wall-shear rate or wall-shear stress increases with the increase in the Reynolds number in the study of Li *et al.*¹² for a drag-reducing turbulent channel flow, since the solution concentration and temperature are constant. In the present study, however, the relation of the wall-shear rate or wall-shear stress and the Reynolds number is not simple, since the solution concentration and temperature are not constant and the streamwise locations are different. Figure 8(b) shows that for all the solution concentration tested $C=65, 100,$ and 150 ppm at $T=20$ °C, the DR monotonically increases with the decrease in the wall-shear rate $\dot{\gamma}_w$ which corresponds to the increase in both the streamwise distance x and Reynolds number Re_θ . In this process, it can be deduced that more rodlike micelles connect to form network structures in the streamwise direction, even if $\dot{\gamma}_w$ becomes smaller. Note that according to the bilayer model³² for the turbulent channel flow, the DR increases with the increase in $\dot{\gamma}_w$ in the stage for the formation of SIS. For both $C=65$ and 100 ppm at $x=1000$ mm, with the increase in solution temperature from $T=25$ to 35 °C, the DR monotonically decreases with the increase in $\dot{\gamma}_w$, which corre-

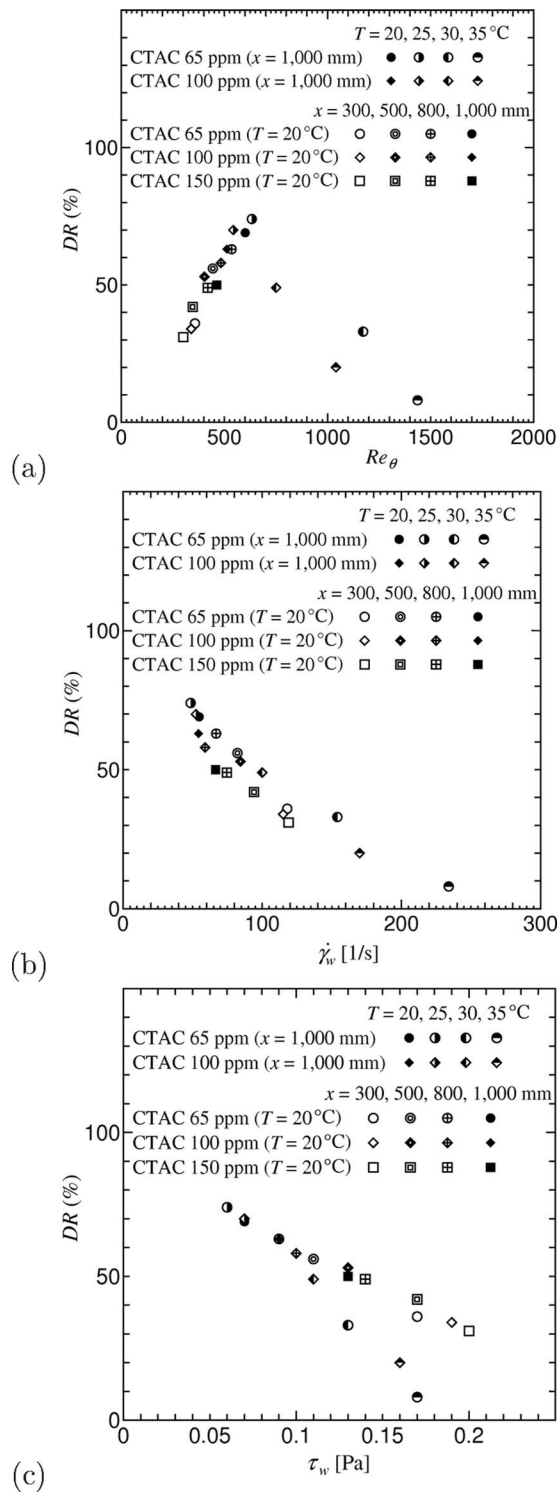


FIG. 8. Drag reduction ratio: (a) vs Reynolds number, (b) vs wall-shear rate, and (c) vs wall-shear stress.

sponds to the increase in the Re_θ for this case. In this process, there is a possibility that the network structures can be gradually broken as the shear rate near the wall becomes larger. As a result, the DR decreases gradually, so the stage for the destruction of SIS seems to be essentially the same as that of the turbulent channel flow even though the experimental conditions are fairly different. However, it should

also be mentioned that the formation and destruction of SIS largely depend on the solution temperature itself, in addition to the wall-shear rate.

Lu *et al.*³³ proposed a schematic micellar phase diagram for a cationic surfactant solution with a constant concentration under different temperatures and shear conditions. According to their diagram, the SIS (threadlike micellar network) cannot be formed at the higher temperature of solutions, even if the wall-shear stress is smaller than the critical wall-shear stress at which the SIS is destroyed. The order of the wall-shear stress, $\tau_w = \rho u_\tau^2$, for the turbulent boundary layer flow in surfactant solutions used is $O(10^{-1})$ Pa [see Fig. 8(c)], while the order of the critical wall-shear stress obtained for the turbulent pipe flow is $O(10^0)$ Pa, as described in Sec. II. This indicates that the wall-shear stress for the present turbulent boundary layer flow is not beyond the critical wall-shear stress. It was also confirmed that the drag reduction ratio for $C=65$ ppm at $T=35^\circ\text{C}$ became larger in the streamwise direction (not shown here). Therefore, it can be deduced that the smaller DR at the higher temperature may be due to the weak or partial formation of SIS, not to the destruction of SIS caused by the large wall-shear stress. The present data are not enough to further discuss the physical mechanism of DR for the turbulent boundary layer flow in surfactant solutions. Interestingly, all data on DR versus the wall-shear rate $\dot{\gamma}_w$ obtained here are collapsed on a single curve [Fig. 8(b)], while the data on DR versus the wall-shear stress τ_w are not [Fig. 8(c)]. For further discussion, experimental data at the small $\dot{\gamma}_w$ ($\dot{\gamma}_w < 50$ 1/s) or τ_w ($\tau_w < 0.05$ Pa) are necessary, making it possible to compare the present data to those of the drag-reducing turbulent channel flow in the flow regime, in which both the drag reduction ratio DR and Reynolds number (i.e., the wall-shear rate or wall-shear stress) increase.

Zakin *et al.*³ also reported that for the drag-reducing turbulent pipe flow, the drag reduction ratio DR was dependent on the diameter of pipe, in addition to the solution concentration and temperature. Quite recently, Gasljevic *et al.*²⁸ thoroughly investigated temporary degradation and recovery of drag-reducing surfactant solutions for the flow through a straight long pipe. These drag-reducing effects for the turbulent pipe flow are unique to the surfactant solution. Future investigations of drag-reducing effects are awaited to determine the turbulent boundary layer flow in surfactant solutions.

Polymer-induced drag reduction is classified into three regimes,^{34,35} referred to as low DR (LDR), high DR (HDR), and maximum DR (MDR). In the present study, the drag reduction ratio DR is $0 < DR < 40\%$ in the LDR regime, $40 \leq DR < 60\%$ in the HDR regime, and $DR \geq 60\%$ in the MDR regime, respectively.

C. Mean velocity

The distribution of the mean velocity scaled by the free-stream velocity U/U_e for $C=100$ and 150 ppm at $T=20^\circ\text{C}$ are shown in Figs. 9(a) and 9(b), respectively. The measurements of U/U_e for surfactant solutions are presented at the locations of $x=300, 500, 800,$ and 1000 mm, while the

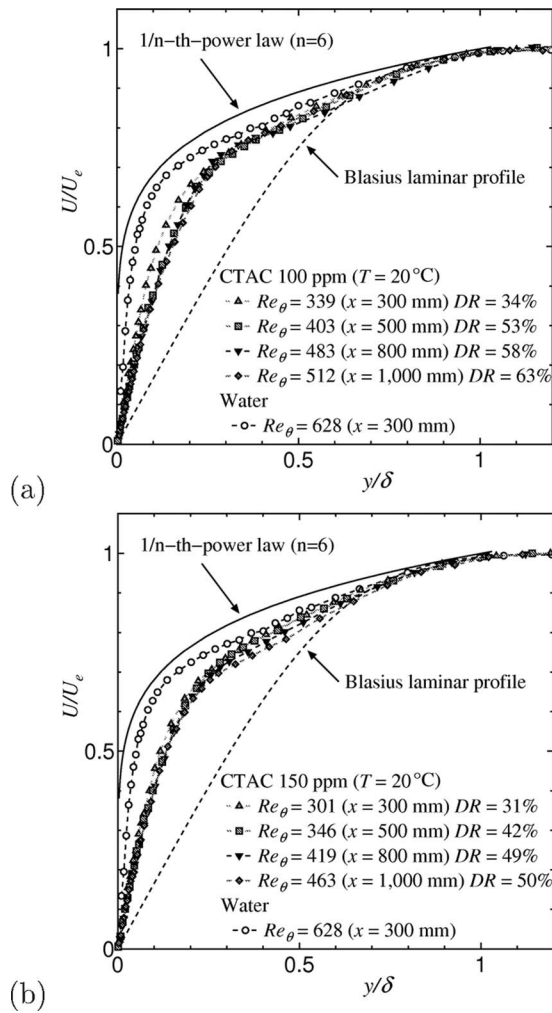


FIG. 9. Mean velocity with outer scaling at $T=20\text{ }^{\circ}\text{C}$: (a) $C=100\text{ ppm}$ and (b) $C=150\text{ ppm}$.

data for water are plotted only at $x=300\text{ mm}$ ($Re_{\theta}=628$). The abscissa y/δ is the distance from the wall scaled by the boundary layer thickness δ . The solid and dashed lines in the figure represent $1/n$ th-power law ($n=6$) and the Blasius laminar profile,³⁰ respectively. The mean velocities U/U_e near the wall for the surfactant solution of $C=100$ and 150 ppm , whose profiles are collapsed for the different Reynolds numbers Re_{θ} and drag reduction ratio DR, are about in the middle between the mean velocity profile of water and the Blasius laminar profile. It is noticeable that the profile of U/U_e at $DR=31$ and 34% (in the LDR regime) is similar to U/U_e at $DR=63\%$ (in the MDR regime).

Figures 10(a) and 10(b) show the mean velocity U/U_e at $x=1000\text{ mm}$ for $C=65$ and 100 ppm at $T=20, 25, 30,$ and $35\text{ }^{\circ}\text{C}$, while the data at $x=1000\text{ mm}$ for water are plotted only at $T=25\text{ }^{\circ}\text{C}$ ($Re_{\theta}=1141$). The U/U_e near the wall at $T=20$ and $25\text{ }^{\circ}\text{C}$ ($DR>60\%$) for both $C=65$ and 100 ppm are about in the middle between the mean velocity profile of water and the Blasius laminar profile. The U/U_e at $T=35\text{ }^{\circ}\text{C}$ for $C=65\text{ ppm}$ ($DR=8\%$, $Re_{\theta}=1437$) and 100 ppm ($DR=20\%$, $Re_{\theta}=1,041$) almost agrees with that for water. The mean velocity U/U_e at $T=30\text{ }^{\circ}\text{C}$ for $C=100\text{ ppm}$ ($DR=49\%$, $Re_{\theta}=751$) is between the U/U_e

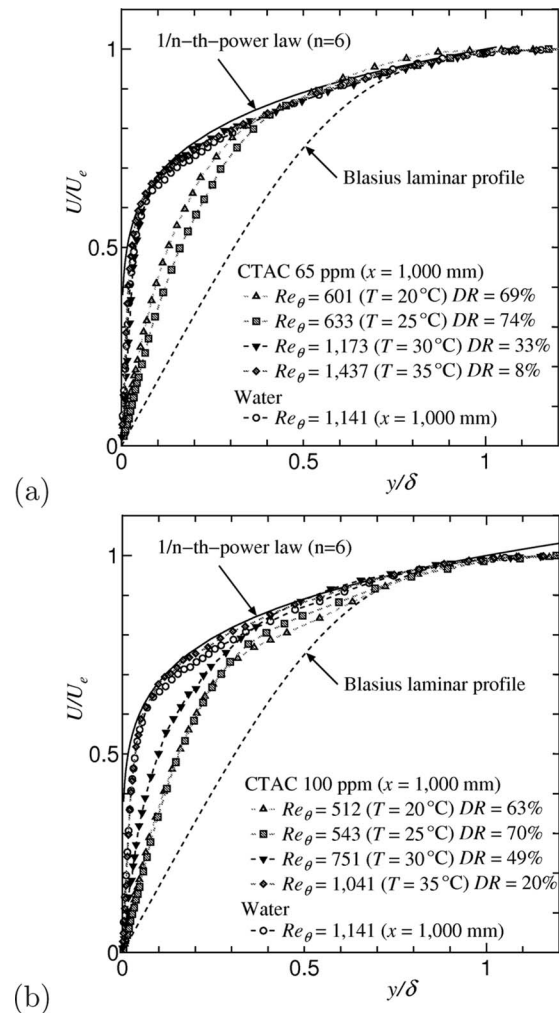


FIG. 10. Mean velocity with outer scaling at $x=1000\text{ mm}$: (a) $C=65\text{ ppm}$ and (b) $C=100\text{ ppm}$.

at $T=25\text{ }^{\circ}\text{C}$ ($DR=70\%$, $Re_{\theta}=543$) and the U/U_e at $T=35\text{ }^{\circ}\text{C}$ ($DR=20\%$, $Re_{\theta}=1,041$). It is found that the profile U/U_e agrees with that for water in the LDR regime, approaches the Blasius laminar profile with the increase in DR in the HDR regime, and exists between the mean velocity profile of water and the Blasius laminar profile in the MDR regime. However, we cannot discriminate the effect of the drag reduction ratio DR from that of the Reynolds number. Experiments for the higher Reynolds numbers $Re_{\theta}>1000$ with the higher drag reduction ratio $DR>60\%$ are required for further discussion.

Figures 11(a) and 11(b) show the profiles of the mean velocity $U^+=U/u_{\tau}$ in the wall-coordinate $y^+=u_{\tau}y/\nu$ at $x=300, 500, 800,$ and 1000 mm for $C=100$ and 150 ppm at $T=20\text{ }^{\circ}\text{C}$, respectively. Figures 12(a) and 12(b) show the profiles of the mean velocity U^+ at $T=20, 25, 30,$ and $35\text{ }^{\circ}\text{C}$ for $C=65$ and 100 ppm at $x=1000\text{ mm}$, respectively. These figures present the linear profile $U^+=y^+$, the log-law profile ($U^+=2.44 \ln y^++5.0$), and Virk's ultimate profile¹ ($U^+=11.7 \ln y^+-17$). For all the surfactant solutions tested, with the increase in the DR, the value of U^+ at $y^+>10$ for surfactant solutions increases, and the slope of U^+ in the HDR and MDR regimes ($DR>40\%$) becomes larger. On the

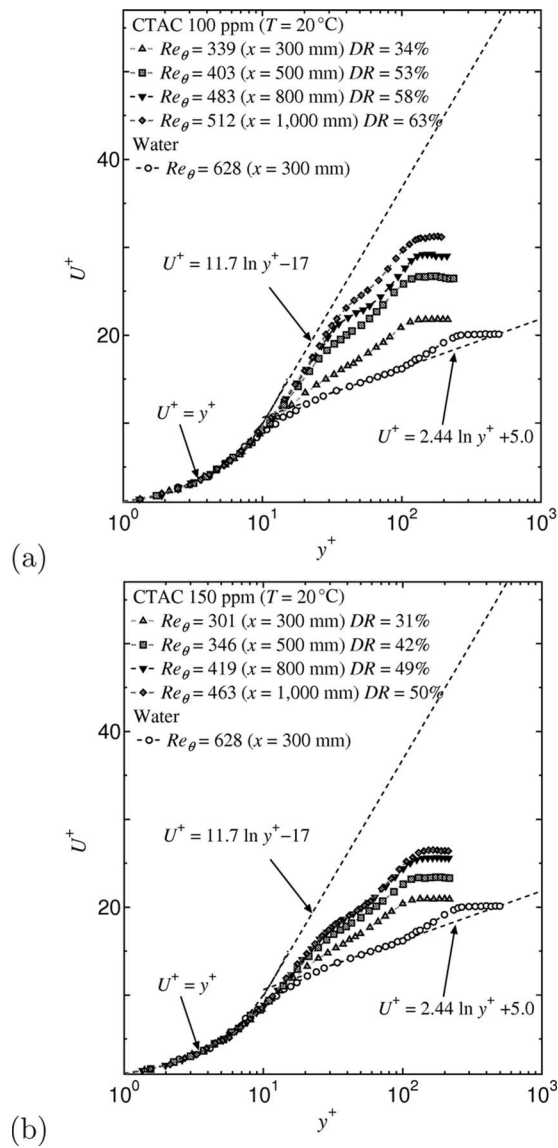


FIG. 11. Mean velocity in wall coordinates at $T=20^\circ\text{C}$: (a) $C=100$ ppm and (b) $C=150$ ppm.

other hand, in the LDR regime ($DR < 40\%$), the U^+ shifts upward in the logarithmic region but its slope is almost the same as that for water, except that the slopes for $C=100$ ppm ($DR=34\%$, $Re_\theta=339$) and $C=150$ ppm ($DR=31\%$, $Re_\theta=301$) at $x=300$ mm and $T=20^\circ\text{C}$ are slightly larger than that of water. This exception may be due to the low Reynolds number effect. It is known that the mean velocity U^+ can be larger than Virk's ultimate profile in the maximum drag-reducing flow of surfactant solutions.^{7,10} For $C=100$ and 150 ppm at $T=20^\circ\text{C}$, the mean velocity U^+ does not exceed Virk's ultimate profile under the present experimental condition (Fig. 11), while the U^+ at $T=25^\circ\text{C}$ for $C=65$ ppm ($DR=74\%$) and $C=100$ ppm ($DR=70\%$) obviously exceed Virk's ultimate profile (Fig. 12). As a whole, the profile of the mean velocity U^+ at $y^+ > 10$ shifts up with the increase in the amount of drag reduction, which seems to be independent of the Reynolds number, streamwise loca-

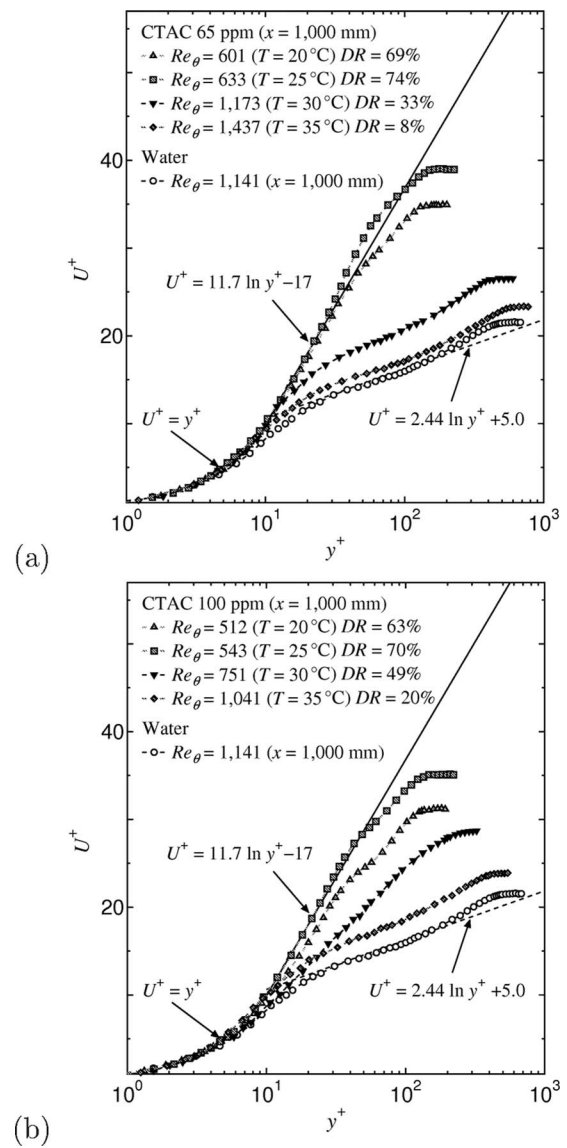


FIG. 12. Mean velocity in wall coordinates at $x=1000$ mm: (a) $C=65$ ppm and (b) $C=100$ ppm.

tion, solution concentration, and temperature. These results are consistent with the previous experimental and numerical studies.^{22,34}

D. Streamwise turbulence intensity

Figures 13(a) and 13(b) show the distributions of streamwise turbulence intensities scaled by friction velocity $u'_{rms} = u'_{rms}/u_\tau$ at $x=300, 500, 800,$ and 1000 mm and $T=20^\circ\text{C}$ for $C=100$ and 150 ppm, respectively. Figures 14(a) and 14(b) show the distribution of u'_{rms} at $T=20, 25, 30,$ and 35°C and $x=1000$ mm for $C=65$ and 100 ppm, respectively. It has been reported that the peak values of u'_{rms} for large drag reduction were larger than that for water at high Reynolds numbers, and smaller at low Reynolds numbers in literature.^{10,19,35} The present data of u'_{rms} at various Reynolds numbers under different concentrations and temperatures indicate that the near-wall maximum is not related to the drag reduction ratio directly [see Fig. 15(a) in

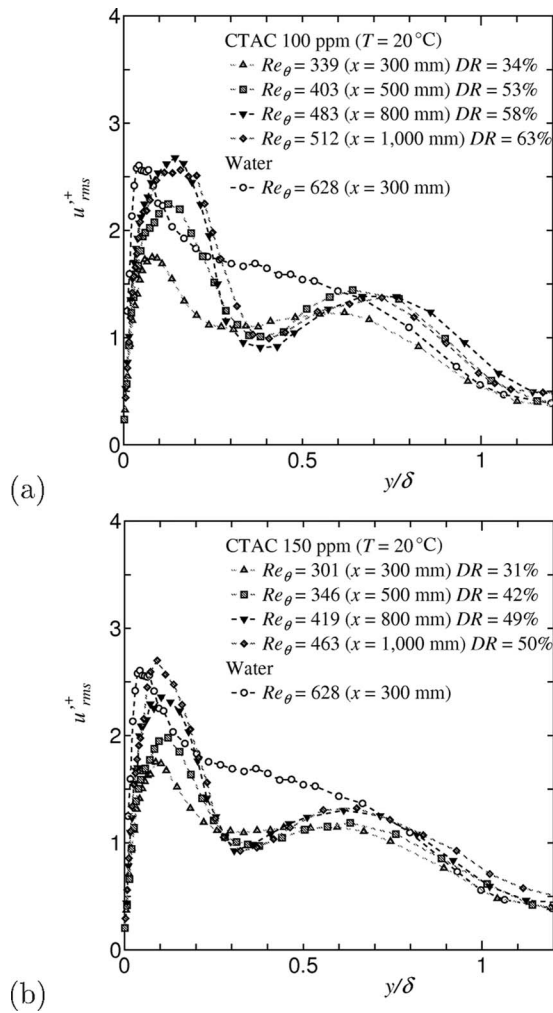


FIG. 13. Streamwise turbulence intensity at $T=20^\circ\text{C}$: (a) $C=100$ ppm and (b) $C=150$ ppm.

detail]. This may be because the Reynolds numbers are different, and this indicates that the development process of the boundary layer is complex owing to the history effect of the surfactant micelles-turbulence interaction, as reported in the study of Hou *et al.*²¹ on the turbulent boundary layer of polymer solutions. In the turbulent channel flow of surfactant solutions, it has also been reported that the dependence of turbulence intensity of the streamwise velocity fluctuations on the Reynolds number and the drag reduction ratio was complex.¹² On the other hand, the value of y/δ at the maximum of u'_{rms+} for surfactant solutions seems to be larger or comparable, compared to that for water (see Fig. 16 in detail), as reported in the literature.^{4,10} Even if the DR for two cases under the different experimental conditions are almost the same (e.g., $DR=33\%$ [Fig. 14(a)] and $DR=34\%$ [Fig. 13(a)]), the profiles of u'_{rms+} are much different from each other, except that the profile of u'_{rms+} at $x=1000$ mm for $C=65$ ppm ($DR=69\%$, $Re_\theta=601$) agrees well with that for $C=100$ ppm ($DR=70\%$, $Re_\theta=543$) in the MDR regime. For the drag-reducing turbulent channel flow in aqueous surfactant solutions, Li *et al.*¹² also reported that the flows at different Reynolds numbers behaved differently in turbulence statistics regardless of similar drag reduction levels. In

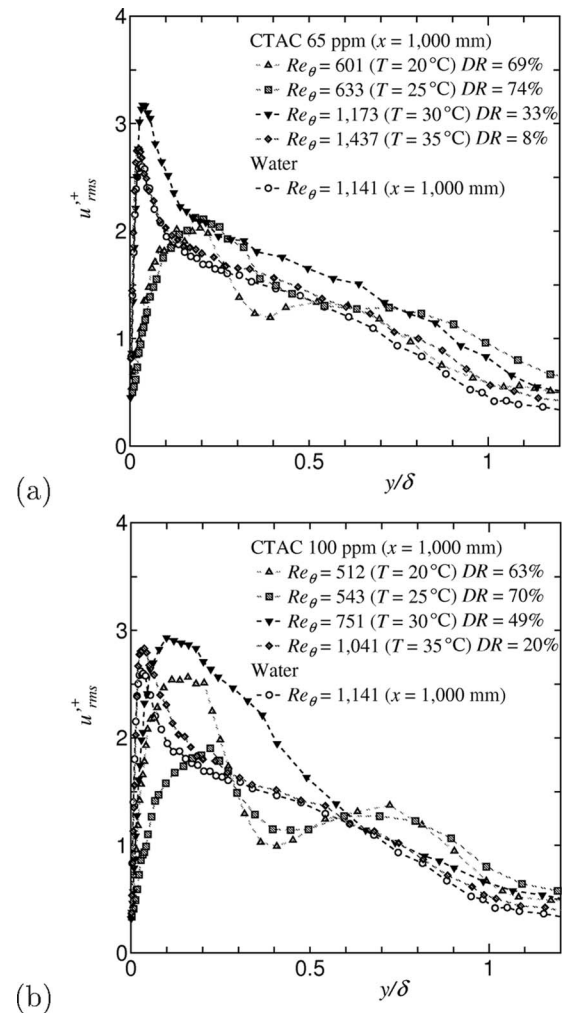


FIG. 14. Streamwise turbulence intensity at $x=1000$ mm: (a) $C=65$ ppm and (b) $C=100$ ppm.

the present study, the Reynolds numbers at two sets of experimental data with similar DR, i.e., $DR=34\%$ and 33% , are $Re_\theta=339$ and 1173 , respectively. The wall-shear rates at $Re_\theta=339$, $DR=34\%$, and $Re_\theta=1173$, $DR=33\%$ were 115 and 154, respectively [see also Fig. 8(b)]. Therefore, this seeming discrepancy in u'_{rms+} for the turbulent boundary layer flow seems to be due to the difference in the wall-shear rate which results in the difference in formation and destruction of SIS near the wall, as well as for the turbulent channel flow. As mentioned in Sec. III B, however, the formation and destruction of SIS are largely dependent on the solution temperature itself, even at the same wall-shear stress.³³ Taking into account that the wall-shear stress for the boundary layer flow is an order of magnitude smaller than the critical wall-shear stress obtained for the turbulent pipe flow, the discrepancy in u'_{rms+} may be due to the weak or partial formation of SIS, not to the destruction of SIS. For further discussion, measurements are needed at both the higher Re_θ and DR and the smaller Re_θ and DR.

Figures 15(a)–15(d) show the near-wall maximum of streamwise turbulence intensity $(u'_{rms+})_{\text{first max}}$ versus the streamwise location x , the wall-shear rate $\dot{\gamma}_w$, the Reynolds number Re_θ , and the drag reduction ratio DR, respectively. It

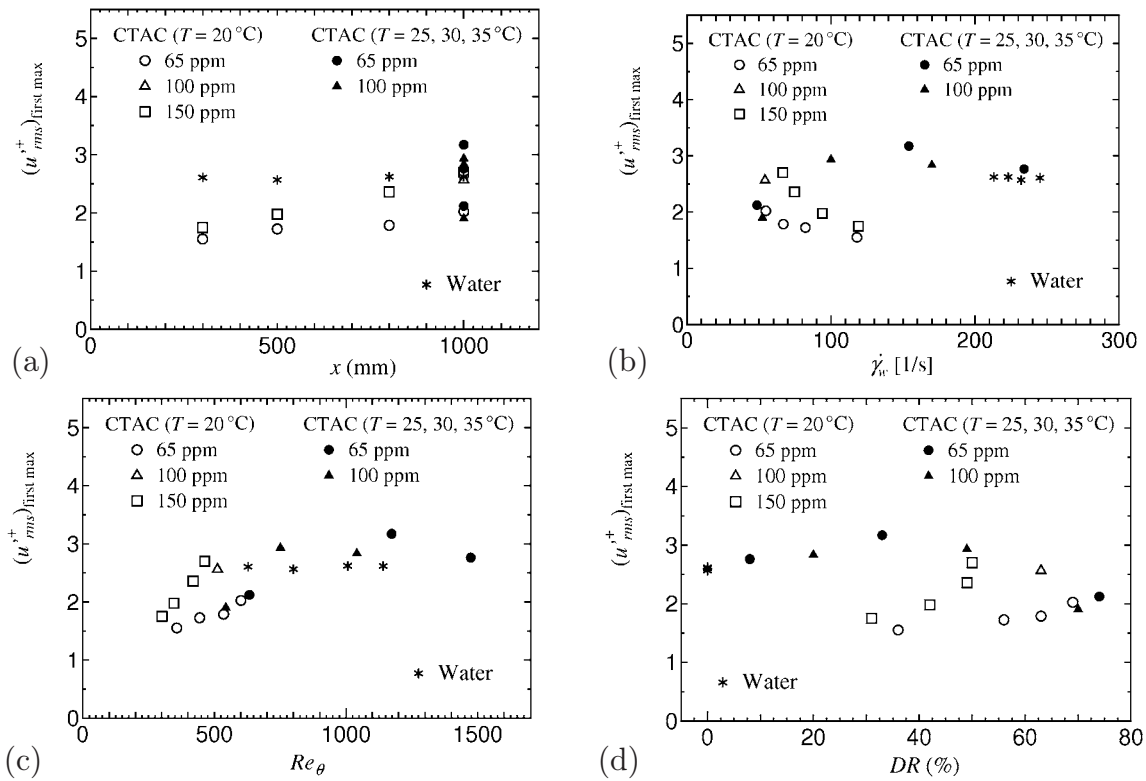


FIG. 15. Maximum of streamwise turbulence intensity near the wall: (a) vs x , (b) vs $\dot{\gamma}_w$, (c) vs Re_{θ} , and (d) vs DR.

is observed that there is no distinct relation between $(u'_{rms})_{first max}^{+}$ versus x , $\dot{\gamma}_w$, Re_{θ} , and DR. This means that the drag-reducing turbulent boundary layer flow of homogeneous surfactant solutions is fairly complex, as mentioned

above. Figures 16(a)–16(d) show the wall-normal location of $(u'_{rms})_{first max}^{+}$, $(y/\delta)_{first max}$, versus the x , $\dot{\gamma}_w$, Re_{θ} , and DR, respectively. The $(y/\delta)_{first max}$ for surfactant solutions seems to approach the data for water as the wall-shear rate $\dot{\gamma}_w$ in-

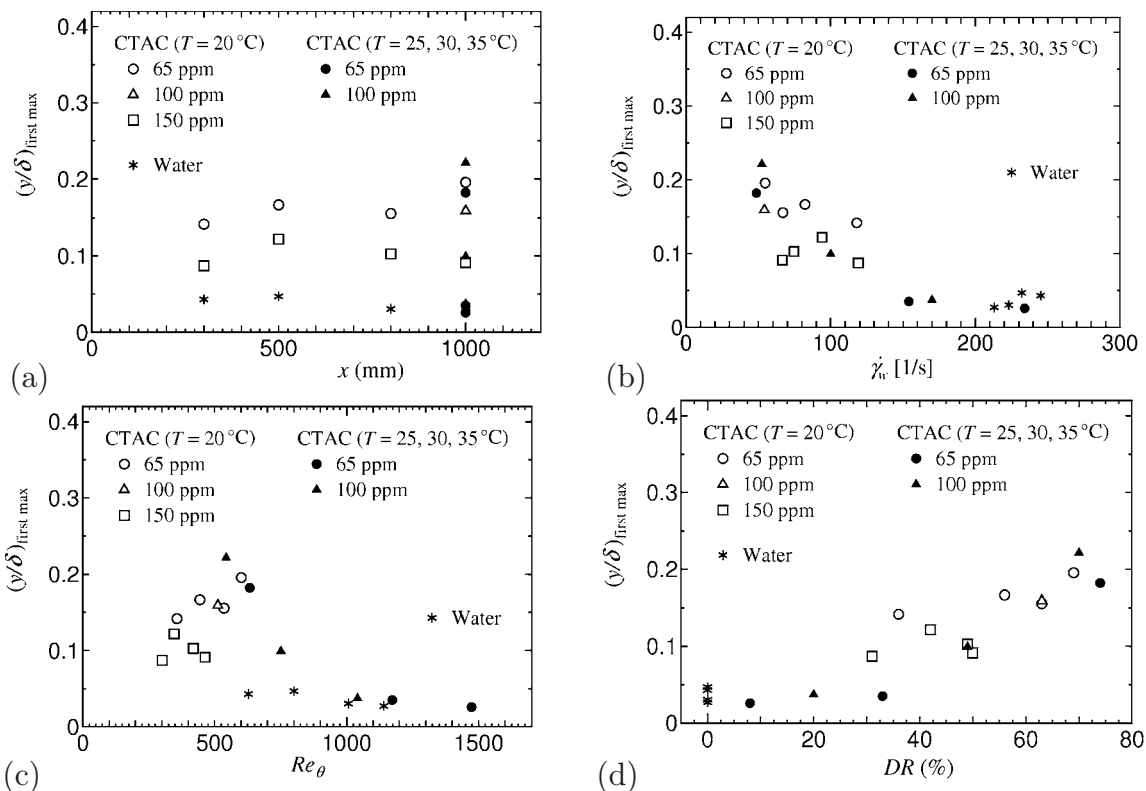


FIG. 16. Wall-normal location of near-wall maximum of streamwise turbulence intensity: (a) vs x , (b) vs $\dot{\gamma}_w$, (c) vs Re_{θ} , and (d) vs DR.

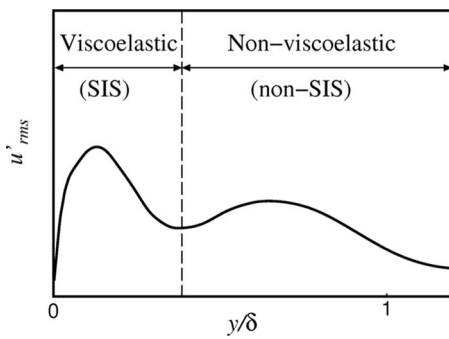


FIG. 17. Bilayered structure model with viscoelastic and nonviscoelastic fluids.

creases and the drag reduction ratio DR decreases, but no distinct relation can be observed between $(y/\delta)_{\text{first max}}$ and x . As the Reynolds number Re_θ increases, the $(y/\delta)_{\text{first max}}$ roughly increases, and then reaches the maximum. After that, it decreases monotonically and approaches the water.

In our previous study²³ ($C=65$ ppm, $T=20$ °C), it was reported that the additional maximum appeared near the center of the boundary layer. In the present study at $T=20$ °C for $C=100$ and 150 ppm (see Fig. 13), the additional maximum can also be observed at different streamwise locations except for the case at $x=300$ mm for $C=150$ ppm. Moreover, the additional maximum observed for $C=100$ and 150 ppm is more distinct than that for $C=65$ ppm.²³ At the higher temperature $T=25$ °C, the additional maximum of u'_{rms} at $x=1000$ mm can be observed for $C=100$ ppm, not for $C=65$ ppm (see Fig. 14). At $T=30$ and 35 °C, the additional maximum at $x=1000$ mm is not observed for both $C=65$ and 100 ppm, in which the DR is relatively small and the Re_θ is relatively large. Here, in order to explain the additional maximum of u'_{rms} , we propose the bilayered structure model for the turbulent boundary layer of surfactant solutions in Fig. 17. In the near-wall region where the mean velocity gradient is large, the flow is in SIS and viscoelastic. On the other hand, in the region away from the wall where the potential and turbulent flows are mixing, the flow is in non-SIS and nonviscoelastic. This may result in the appearance of the additional maximum of the streamwise turbulence intensity. The bilayered structure model seems to be similar to the bilayer model proposed by Yu and Kawaguchi³² for the DNS of the drag-reducing turbulent channel flow by surfactant additives with Newtonian and non-Newtonian fluid coexistence. However, as described in Sec. III B, for the turbulent boundary layer in surfactant solutions with constant concentration and temperature, more rodlike micelles connect to form network structures in the streamwise direction, even if $\dot{\gamma}_w$ becomes smaller, while for the turbulent channel flow, more rodlike micelles connect to form network structures as the Reynolds number increases, i.e., the wall-shear rate increases in flow B in their bilayer model.³²

The present model is based on the measurements of shear viscosity, in which the SIS can be observed at $T=20$ and 25 °C, not at $T=30$ and 35 °C (see Fig. 2), considering that the additional maximum is observed at $T=20$ and

25 °C, not at $T=30$ and 35 °C (see Figs. 13 and 14), except that the SIS is observed at $T=35$ °C for $C=100$ ppm. However, we cannot deny the possibility that the additional maximum is due to the low Reynolds number effect because experimental data are lacking at the higher Reynolds numbers $Re_\theta > 1000$ with the higher drag reduction ratio $DR > 50\%$ or the smaller Reynolds number $Re_\theta < 500$ with the smaller drag reduction ratio $DR < 20\%$, which is beyond the scope of this paper. Although Hou *et al.*²¹ reported that the $u'_{\text{rms}}/(\nu_\tau U_e)$ profiles with the mixed inner and outer velocity scalings for polymer solutions were collapsed with the Newtonian profiles, the existence of the additional maximum does not depend on the normalization of streamwise turbulence intensity.

Figures 18(a)–18(d) show the additional maximum of streamwise turbulence intensity near the center of the boundary layer $(u'_{\text{rms}})_{\text{second max}}$ versus the streamwise location x , the wall-shear rate $\dot{\gamma}_w$, the Reynolds number Re_θ , and the drag reduction ratio DR, respectively. It can be known that the additional maximum $(u'_{\text{rms}})_{\text{second max}}$ appears only at the small wall-shear rate ($\dot{\gamma}_w < 120$), at the small Reynolds number ($Re_\theta \leq 600$), and roughly in the HDR and MDR regimes ($DR > 30\%$). It is also found that the $(u'_{\text{rms}})_{\text{second max}}$ is between 1.2 and 1.5, which is independent of the x , $\dot{\gamma}_w$, Re_θ , and DR. Figures 19(a)–19(d) show the wall-normal location of $(u'_{\text{rms}})_{\text{second max}}$, $(y/\delta)_{\text{second max}}$, versus the x , $\dot{\gamma}_w$, Re_θ , and DR, respectively. The $(y/\delta)_{\text{second max}}$ is between 0.5 and 0.7, which seems to be independent of the abscissa.

E. Wall-normal turbulence intensity

Figures 20(a) and 20(b) show the distributions of wall-normal turbulence intensities scaled by friction velocity v'_{rms} at $x=300, 500, 800,$ and 1000 mm and $T=20$ °C for $C=100$ and 150 ppm, respectively. The wall-normal turbulence intensity v'_{rms} for the surfactant solution of both $C=100$ and 150 ppm is much smaller than that for water and is virtually constant across the boundary layer. In addition, the peak of v'_{rms} seen in the canonical wall turbulence does not appear for the surfactant solution. Although these trends are similar to that for the drag-reducing turbulent channel flow of surfactant solutions,^{4,10} it should be noted that the v'_{rms} is virtually constant even in the LDR regime ($DR < 40\%$), which may be due to the low Reynolds number effect, as mentioned above.

Figures 21(a) and 21(b) show the distributions of v'_{rms} at $T=20, 25, 30,$ and 35 °C and $x=1000$ mm for $C=65$ and 100 ppm, respectively. For $C=65$ ppm, the v'_{rms} at $T=20$ and 25 °C ($DR=69\%$ and 74%) in the MDR regime are almost constant and half that of water, as reported for the drag-reducing turbulent channel flow in surfactant solutions.^{4,10} On the other hand, the v'_{rms} at $T=30$ and 35 °C ($DR=33\%$ and 8%) in the LDR regime are larger than that for water. For $C=100$ ppm, the v'_{rms} at $T=20$ and 25 °C ($DR=63\%$ and 70%) in the MDR regime is almost constant and half that of water, while the v'_{rms} at $T=35$ °C ($DR=20\%$) in the LDR regime is comparable with that for water. The v'_{rms} at

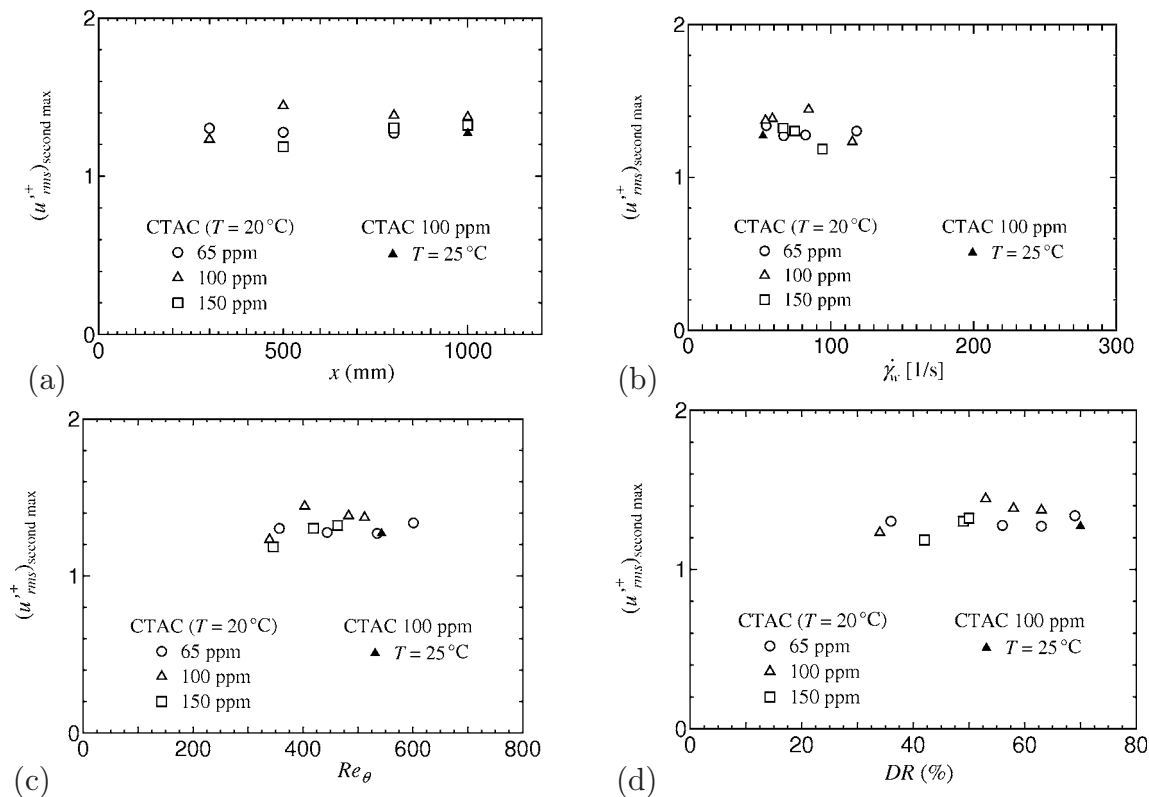


FIG. 18. Additional maximum of streamwise turbulence intensity near the center of boundary layer: (a) vs x , (b) vs $\dot{\gamma}_w$, (c) vs Re_θ , and (d) vs DR .

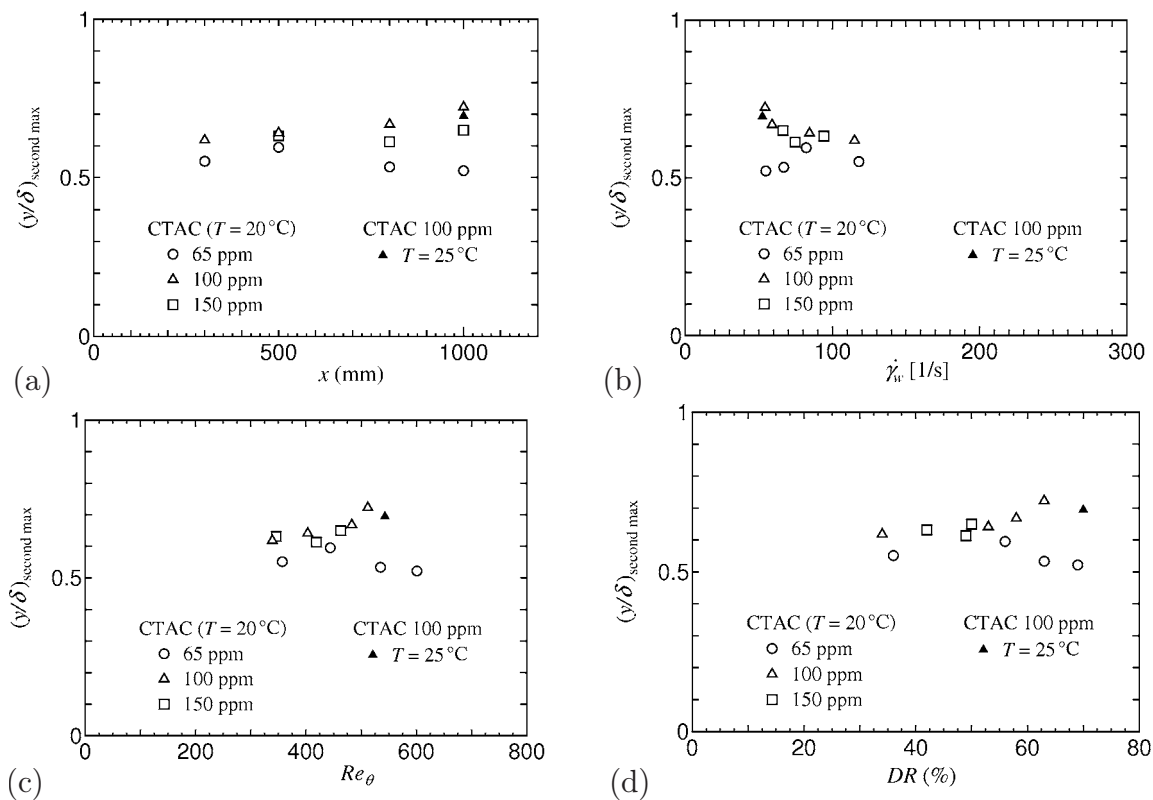


FIG. 19. Wall-normal location of additional maximum of streamwise turbulence intensity near the center of boundary layer: (a) vs x , (b) vs $\dot{\gamma}_w$, (c) vs Re_θ , and (d) vs DR .

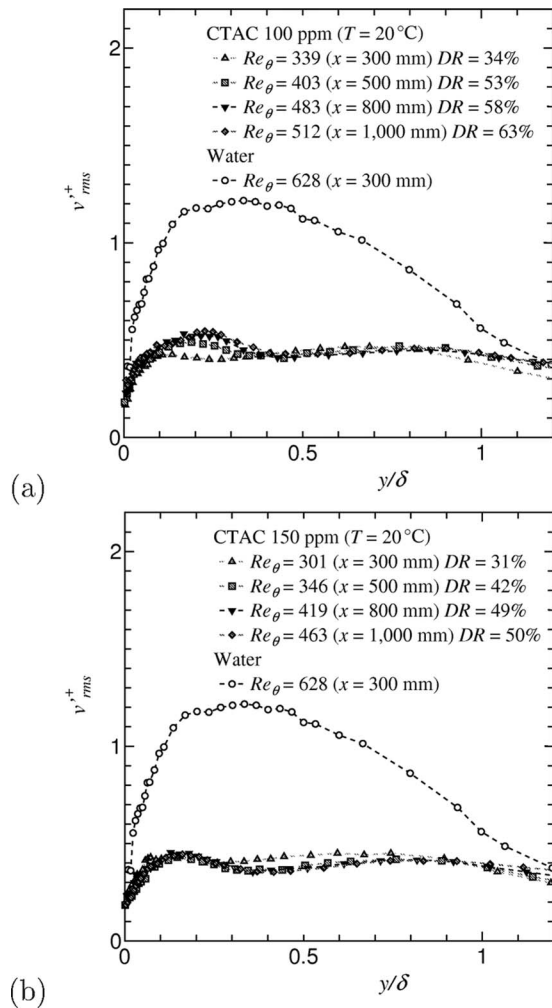


FIG. 20. Wall-normal turbulence intensity at $T=20\text{ }^{\circ}\text{C}$: (a) $C=100\text{ ppm}$ and (b) $C=150\text{ ppm}$.

$T=30\text{ }^{\circ}\text{C}$ ($DR=49\%$) in the HDR regime is about in the middle between v'^+_{rms} at $T=25\text{ }^{\circ}\text{C}$ ($DR=70\%$) and $35\text{ }^{\circ}\text{C}$ ($DR=20\%$).

F. Reynolds shear stress

Figures 22(a) and 22(b) show the distributions of Reynolds shear stress scaled by the friction velocity $-u'v'^+$ at $x=300, 500, 800,$ and 1000 mm and $T=20\text{ }^{\circ}\text{C}$ for $C=100$ and 150 ppm , respectively. The Reynolds shear stress is reportedly almost zero for the drag-reducing turbulent channel flow of surfactant solutions at the large drag reduction ratio.^{4,10} Reynolds shear stress for the surfactant solutions of $C=100$ and 150 ppm is almost zero across the boundary layer, which is independent of the amount of the drag reduction. Note that the Reynolds shear stress is almost zero even in the LDR regime ($DR < 40\%$). This may be due to the low Reynolds number effect, as mentioned above.

Figures 23(a) and 23(b) show the distributions of $-u'v'^+$ at $T=20, 25, 30,$ and $35\text{ }^{\circ}\text{C}$ and $x=1000\text{ mm}$ for $C=65$ and 100 ppm , respectively. For both $C=65$ and 100 ppm , the $-u'v'^+$ at $T=20$ and $25\text{ }^{\circ}\text{C}$ ($DR > 60\%$) in the MDR regime is close to zero across the boundary layer, in which the wall-normal turbulence intensity v'^+_{rms} is almost constant and half

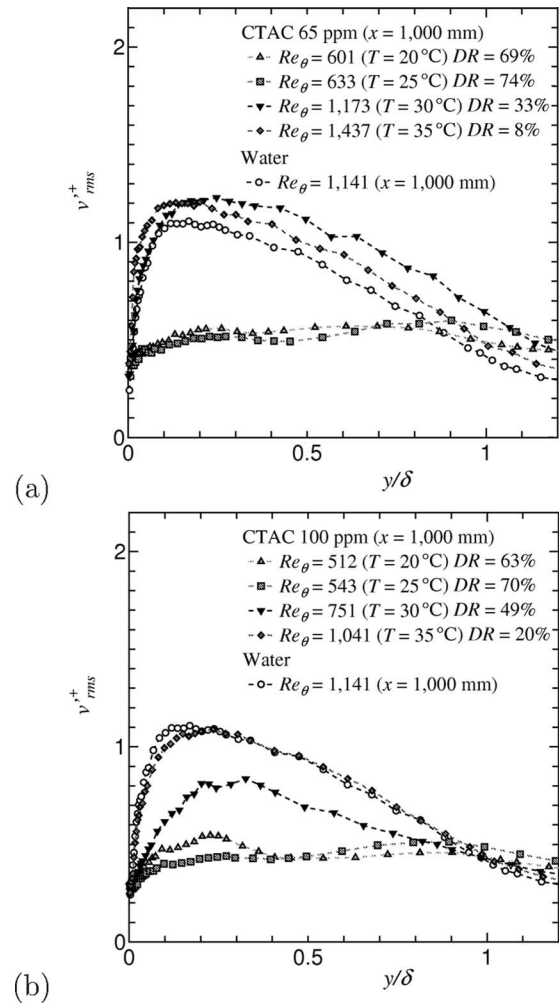


FIG. 21. Wall-normal turbulence intensity at $x=1000\text{ mm}$: (a) $C=65\text{ ppm}$ and (b) $C=100\text{ ppm}$.

that of water. In a recent study²¹ on the drag-reducing turbulent boundary layer with polymer injection, it has also been reported that the Reynolds shear stress for the drag-reducing turbulent boundary layer flow is larger compared to water. For $C=65\text{ ppm}$, compared to data on water, the $-u'v'^+$ in the LDR regime is somewhat larger at $T=30\text{ }^{\circ}\text{C}$ ($DR=33\%$), and is almost the same at $T=35\text{ }^{\circ}\text{C}$ ($DR=8\%$), which corresponds to the result that the streamwise turbulence intensity u'^+_{rms} is larger at $T=30\text{ }^{\circ}\text{C}$ and is almost the same at $T=35\text{ }^{\circ}\text{C}$. For $C=100\text{ ppm}$, compared to data on water, the $-u'v'^+$ is somewhat smaller at $T=30\text{ }^{\circ}\text{C}$ ($DR=49\%$) in the HDR regime, and is almost the same at $T=35\text{ }^{\circ}\text{C}$ ($DR=20\%$) in the LDR regime.

Comparing Figs. 13 and 14 and Figs. 12 and 23, it is revealed that when the Reynolds shear stress is almost zero across the boundary layer, the streamwise turbulence intensity has the additional maximum near the center of the boundary layer in addition to the near-wall maximum.

IV. PIV MEASUREMENTS

A. Statistics

To show the accuracy of the present PIV measurements for both water and surfactant solution $C=100\text{ ppm}$, the mean velocity U/U_e , streamwise and wall-normal turbulence

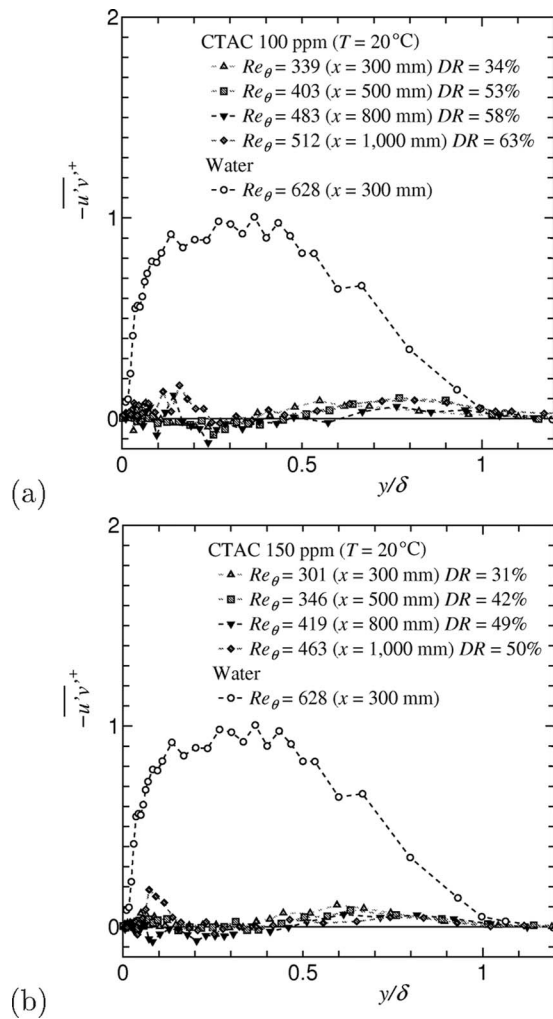


FIG. 22. Reynolds shear stress at $T=20^\circ\text{C}$: (a) $C=100$ ppm and (b) $C=150$ ppm.

intensities u'_{rms}/U_e and v'_{rms}/U_e , and Reynolds shear stress $-\overline{u'v'}/U_e^2$ at $x=1000$ mm and $T=20^\circ\text{C}$ were compared to the corresponding data obtained by the LDV measurement in Fig. 24. Note that both coordinates are scaled by outer variables such as U_e and δ . The drag reduction ratio DR for $C=100$ ppm was 63%, which was obtained by the LDV measurement. The DR could not be obtained by the PIV measurement owing to the difficulty of accurate measurement in the region close to the wall ($y/\delta < 0.1$). The profiles of mean velocity for both the water and surfactant solution obtained by the PIV measurement agree well with the corresponding data obtained by the LDV measurement [Fig. 24(a)]. For both the LDV and PIV measurements, the additional maximum of streamwise turbulence intensity in the region $0.5 < y/\delta < 0.7$ can be seen for the surfactant solution [Fig. 24(b)], although the scale of the additional maximum and its wall-normal location are somewhat different, where this difference is within the scatter of the present measurements (see Fig. 18). The PIV measurement also supports the existence of the additional maximum for the turbulent boundary layer of the surfactant solutions. The wall-normal turbulence intensity for the PIV measurement is somewhat smaller than that for the LDV measurement [Fig. 24(c)]. This is due to the

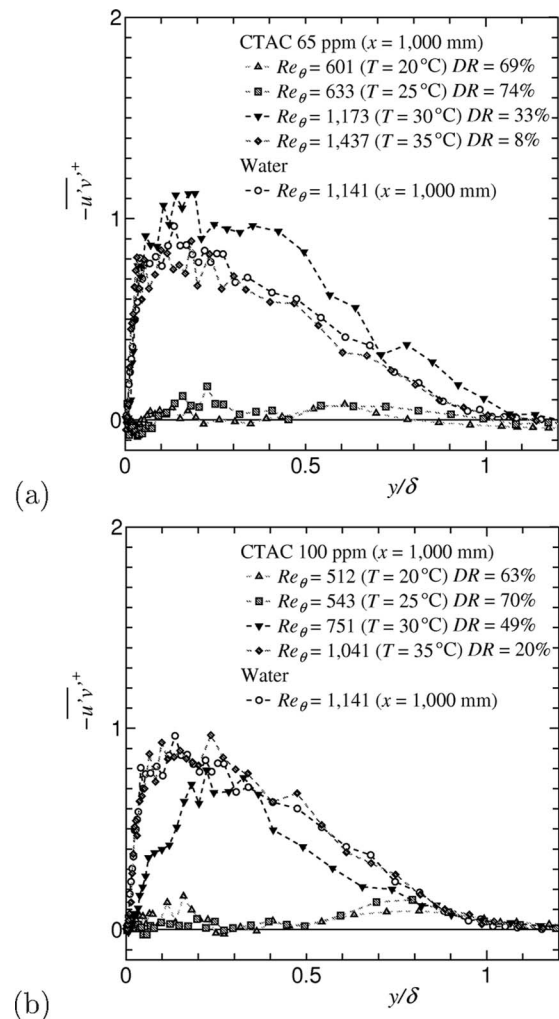


FIG. 23. Reynolds shear stress at $x=1000$ mm: (a) $C=65$ ppm and (b) $C=100$ ppm.

lack of spatial resolution of the PIV measurement, and the same trend has been reported by Warholic *et al.*³⁶ Regarding the Reynolds shear stress which is controlled by large-scale flow structures, the PIV measurements agree well with the LDV measurements for both the water and surfactant solution [Fig. 24(d)], as reported by Baik *et al.*³⁷

B. Fluctuating velocity vector fields

Figure 25 shows the time sequence realization of typical fluctuating velocity vector fields in streamwise and wall-normal ($x-y$) plane for the water. Flow is from left to right. In the figure, x' represents the left end of the image obtained. The vector represents the fluctuating velocity vector. In the figure, for the visibility, the 21 and 50 vectors are plotted in the streamwise and wall-normal directions, respectively. In Fig. 25(a), we can observe two vortex cores (A, B) which seem to constitute a hairpin vortex packet.³⁸ Subsequently, the sweep event (C) appears in Fig. 25(b), and then the new hairpin vortex (D) and the ejection event (E) appear in Fig. 25(c). This kind of process observed for water is consistent with a self-sustaining mechanism of near-wall turbulence³⁹ which has been widely accepted for the Newtonian fluid.

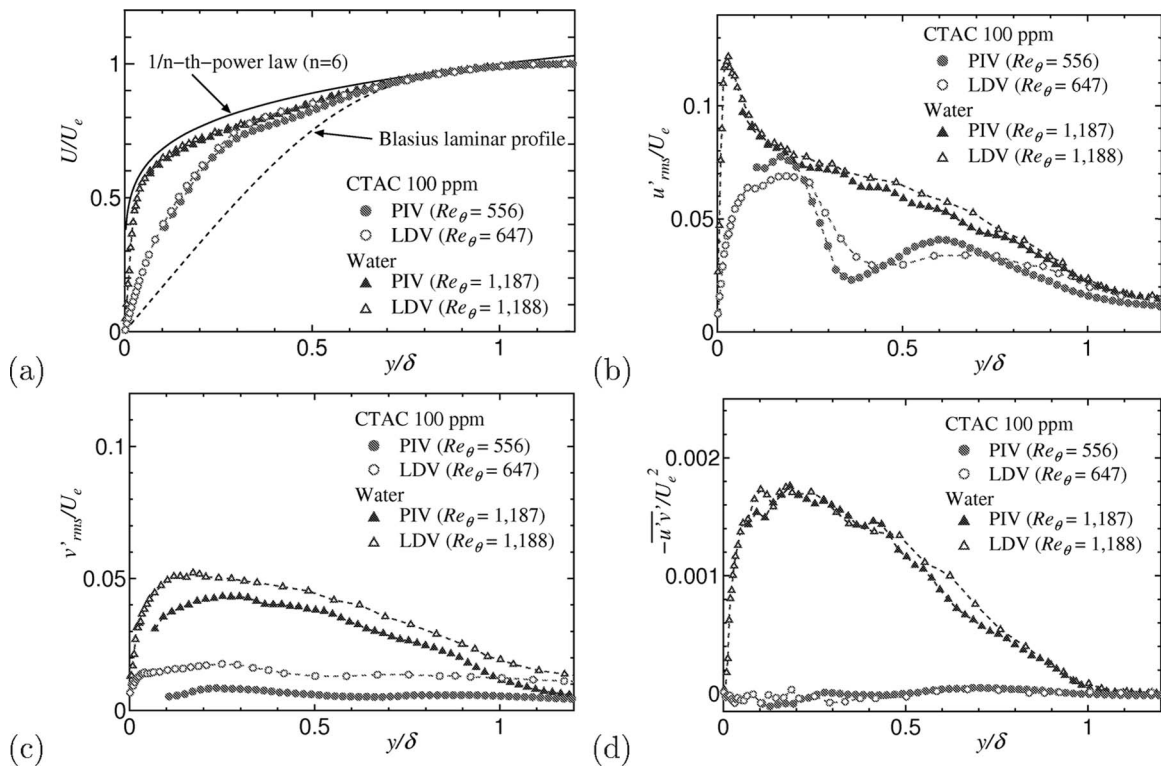


FIG. 24. Comparison of statistics between PIV and LDV measurements at $x=1000$ mm, $T=20$ °C for water and surfactant solution $C=100$ ppm with $DR=63\%$: (a) Mean velocity, (b) streamwise turbulence intensity, (c) wall-normal turbulence intensity, and (d) Reynolds shear stress.

For the surfactant solution of $C=100$ ppm with the $DR=63\%$, we found that the velocity fields frequently show a calm layered appearance, as reported in the study of Baik *et al.*³⁷ who found the layered structures for the heterogeneous drag-reducing channel flow due to the polymer injection. Figures 26 and 27 show the time sequence fluctuating velocity vector fields for $C=100$ ppm in the typical situations with low and high activity, respectively. The arrow scale is the same as that for water. In the case of low activity, the velocity fluctuations are attenuated largely across the turbulent boundary layer, and the hairpin packet and sweep and ejection events are not observed (Fig. 26). On the other hand, in the case of high activity, we can observe the bilayered structure in Fig. 27(a), in which the streamwise velocity fluctuations are relatively large even in the region $0.5 < y/\delta < 0.7$ (F), in addition to the near-wall region (G). In the regions F and G, the fluctuating velocity vectors are almost parallel to the wall and the velocity vectors in both regions are in the positive direction. This turbulence structure is consistent with the two maxima in the streamwise turbulence intensity [see Fig. 24(b)] and the large decrease in the wall-normal turbulence intensity [see Fig. 24(c)]. In literature on polymer solutions,^{36,37} although the bilayered structure has not been observed, the velocity fluctuations were reportedly almost rectilinear for the large drag reduction case. In region (H), the streamwise fluctuating velocity vectors alter the direction, and are almost parallel to the wall. Then, region H becomes larger in the streamwise direction in Fig. 27(b). Eventually, in Fig. 27(c), the fluctuating velocity vectors in regions F and H are almost parallel to the wall and in opposite directions to one another. The contributions of positive

and negative values of $u'v'$ to the Reynolds shear stress should just about balance, which results in the almost zero Reynolds shear stress [see Fig. 24(d)], as reported in polymer solutions.³⁶ In the active situation of the present study, the bilayered structure is dominant and the hairpin packet is not observed. The inhibition of the hairpin vortex in the present study is supported by the recent dynamical simulation of Kim *et al.*^{40,41} for polymer solutions. From the present PIV measurements, it can be concluded that the bilayered structure results in the additional maximum of the streamwise turbulence intensity. As described in Sec. III D, it is speculated that the bilayered structure and the resultant additional maximum of the streamwise turbulence intensity are related to the SIS of the surfactant solution.

V. CONCLUSION AND DISCUSSION

In this work, the influence of a drag-reducing surfactant on the turbulent boundary layer was systematically investigated at various Reynolds numbers from $Re_\theta=301$ to 1437 and the drag reduction ratio from $DR=8\%$ to 74% at locations downstream from the leading edge where $x=300, 500, 800,$ or 1000 mm under different solution concentrations and temperatures using a two-component LDV system. To investigate turbulence structures, the two-dimensional PIV measurements were also performed at $x=1000$ mm. The surfactant solution used here was a mixture of CTAC with sodium salicylate as counterion, which was dissolved in tap water. The concentrations tested were $C=65, 100,$ and 150 ppm, and the temperature of surfactant solution was $T=20, 25, 30,$

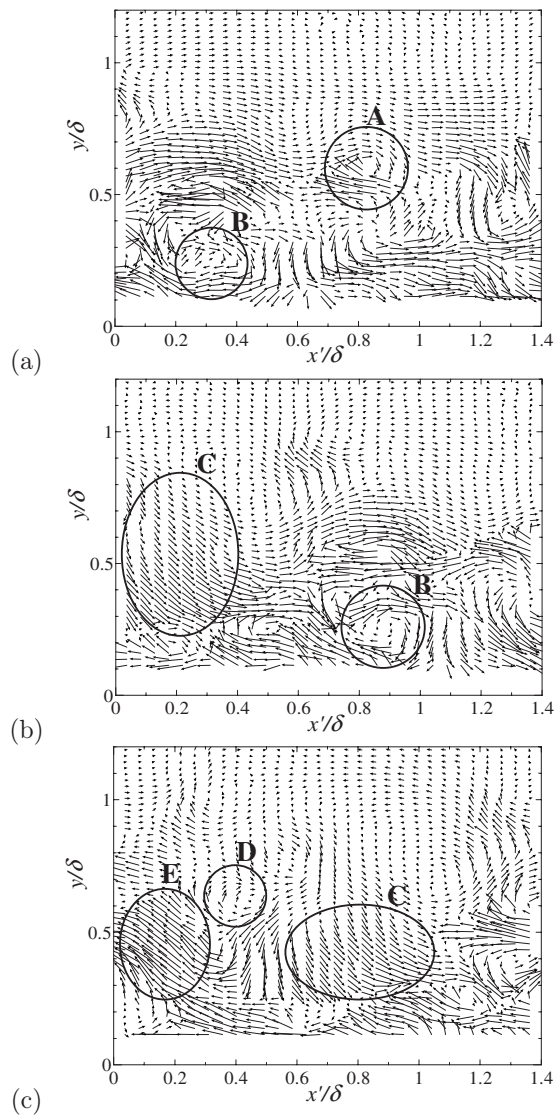


FIG. 25. Fluctuating velocity vector fields in x - y plane for water: (a) $t=t_0$, (b) $t=t_0+0.06$ s, and (c) $t=t_0+0.12$ s. Flow is from left to right.

and 35 °C. The concentration of surfactant solution in the boundary layer flow was homogeneous.

The drag reduction ratio DR at $T=20$ °C becomes larger downstream, and decreases with the increase in C from 65 to 150 ppm. For both $C=65$ and 100 ppm, the DR at $x=1000$ mm becomes smaller with the increase in T from 25 to 35 °C, and the DR at $T=20$ °C is smaller than DR at $T=25$ °C. It was revealed that all data on DR versus the wall-shear rate $\dot{\gamma}_w$ obtained here were collapsed on a single curve. In order to evaluate the mean velocity and turbulence statistics, we introduced three distinct regimes of drag reduction, referred to as LDR ($0 < DR < 40\%$), HDR ($40 \leq DR < 60\%$), and MDR ($DR \geq 60\%$) regimes. It is found that the distributions of the mean velocity could be explained by these three regimes with some exceptions, whereas turbulence statistics could not.

The existence of the additional maximum of the streamwise turbulence intensity near the center of the boundary layer was verified in various experimental conditions. In the present study, the additional maximum, which is observed at

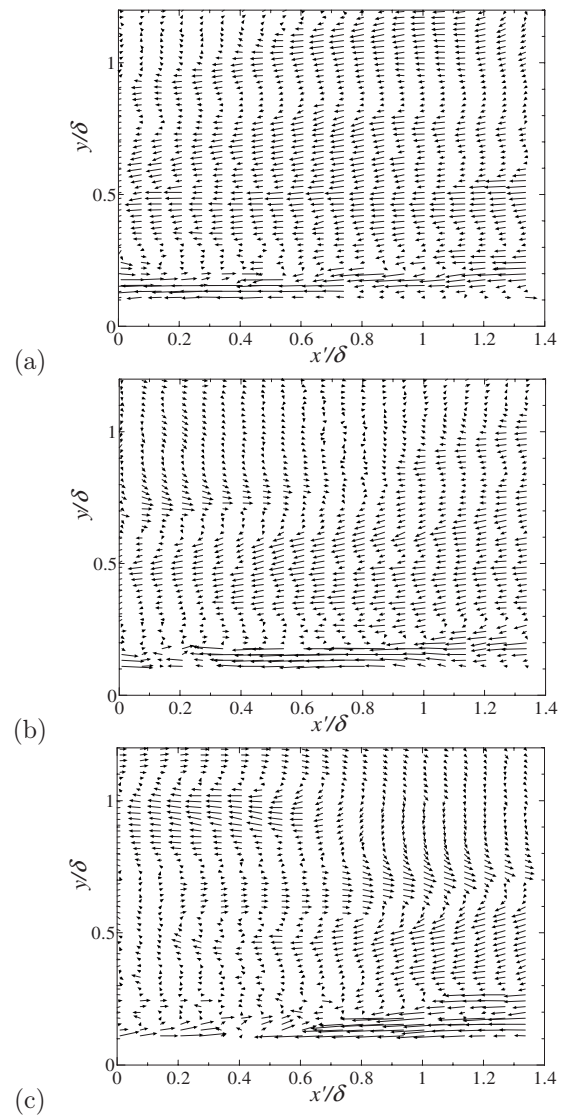


FIG. 26. Fluctuating velocity vector fields in x - y plane for $C=100$ ppm with $DR=63\%$ in the situation with low activity: (a) $t=t_1$, (b) $t=t_1+0.06$ s, and (c) $t=t_1+0.12$ s.

$T=20$ and 25 °C, not at $T=30$ and 35 °C, appears roughly in the HDR and MDR regimes at the relatively low Reynolds numbers. The additional maximum of the streamwise turbulence intensity near the center of the boundary layer and its wall-normal location were independent of the streamwise location x , the wall-shear rate $\dot{\gamma}_w$, the Reynolds number Re_θ , and the drag reduction ratio DR, while no distinct relation between the standard maximum of the streamwise turbulence intensity near the wall $(u'_{rms})_{first\ max}$ versus x , $\dot{\gamma}_w$, Re_θ , and DR could be observed and its wall-normal location becomes more distant from the wall with the increase in DR in the HDR and MDR regimes. We proposed the bilayered structure model in order to explain the additional maximum of the streamwise turbulence intensity. In the near-wall region where the mean velocity gradient is large, the flow is in SIS and viscoelastic. On the other hand, in the region away from the wall where the potential and turbulent flows are mixing, the flow is in non-SIS and nonviscoelastic. This may result in the appearance of the additional maximum of the streamwise

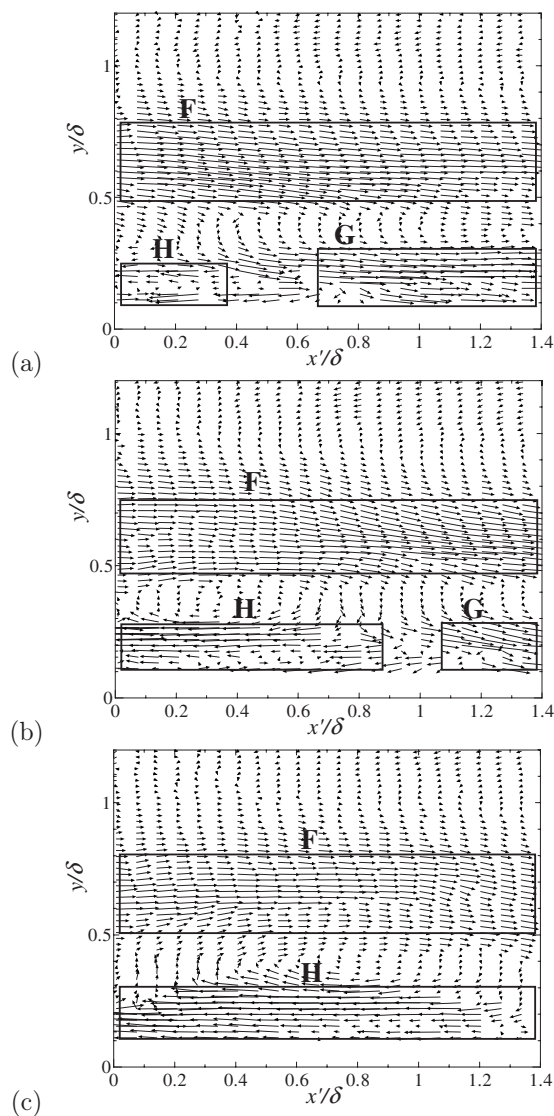


FIG. 27. Fluctuating velocity vector fields in x - y plane for $C=100$ ppm with $DR=63\%$ in the situation with high activity: (a) $t=t_2$ s, (b) $t=t_2+0.06$ s, and (c) $t=t_2+0.12$ s.

turbulence intensity. This model was based on the measurements of the shear viscosity, in which the SIS can be observed at $T=20$ and 25 °C, not at $T=30$ and 35 °C, with one exception. The present model is assumed so that the formation of the SIS in the turbulent flow of the dilute surfactant solution is strongly related to the viscoelasticity and the drag reduction.^{2,3,42} It should be mentioned, however, that Lu *et al.*⁴³ and Lin *et al.*⁴⁴ found that the drag-reducing surfactant solution in which the network structure of rodlike micelles was formed did not necessarily have viscoelasticity, and Gasljevic *et al.*²⁸ proposed the hypothesis of drag reduction being possible without the SIS of very weak surfactant solution. The effect of the SIS or viscoelasticity on the drag reduction should be investigated further.

The PIV measurements revealed that the fluctuating velocity vector fields showed the two situations with low and high activity. In low activity, the velocity fluctuations are attenuated largely across the turbulent boundary layer. In high activity, fluctuating velocity vectors were almost paral-

lel to the wall and relatively large in both regions near the wall and the center of the boundary layer. Therefore, the fluctuating velocity vector fields seem to be a bilayered structure, which has not yet been reported in previous study. It could be concluded that the bilayered structure results in the additional maximum, which supports the bilayered structure model presented.

In a quite recent review,²² the mechanism of drag reduction in polymer solutions has been summarized as follows. The polymers disrupt the near-wall turbulence regeneration cycle and reduce the turbulent friction drag by directly interacting with and dampening the quasistreamwise vortices. The vortex suppression results from spatial gradients in the polymer stress surrounding the vortices that leads to the transfer of energy from the vortices to the polymers. The many physical aspects may be applicable to surfactant solutions. In fact, turbulence statistics and structures in surfactant solutions are generally similar to those in polymer solutions for both turbulent channel and boundary layer flows. It would be very difficult, however, to explain the bilayered structure and the resultant additional maximum of the streamwise turbulence intensity observed in the present study using only the above mechanism for the polymer solution. The bilayered structure model presented here could compensate this issue but could not solve the drag-reducing mechanism for the turbulent boundary layer of surfactant solutions completely. This may be because there is no information on the difference in molecular structures in the flow between the polymer chains and surfactant micelles, although the SIS, which is related to the large-scale structure of micelles, can be observed for the drag-reducing surfactant solution and causes the remarkable difference in the rheological property for the steady shear flow from the drag-reducing polymer solution. Measurements of the relaxation time for formation and destruction of large-scale structures of micelles and the time of their alignment parallel to each other in the boundary layer would also be helpful to explain dynamic phenomena in the turbulent boundary layer. In addition to the further experimental investigation using the LDV and PIV measurements at both high Re with high DR and low Re with low DR, therefore, a numerical investigation on the dynamical interaction between the coherent structures present in the turbulent flows and the surfactant micelles would be required in order to clarify the mechanism of the bilayered structure observed for the drag-reducing surfactant solutions in the present study. To this end, the Brownian dynamic simulations^{45,46} for the drag-reducing turbulent flow may be a promising candidate.

ACKNOWLEDGMENTS

This work was partially supported by a Grant-in-Aid for Scientific Research (No. 19560170) from the Japan Society for the Promotion of Science. Special thanks are also due to S. Takeuchi and J. Suzuki for their unfailing assistance with the experimental measurements.

¹P. S. Virk, "Drag reduction fundamentals," *AICHE J.* **21**, 625 (1975).

²A. Gyr and H.-W. Bewersdorff, *Drag Reduction of Turbulent Flows by Additives* (Kluwer Academic, Dordrecht, The Netherlands, 1995).

- ³J. L. Zakin, B. Lu, and H.-W. Bewersdorff, "Surfactant drag reduction," *Rev. Chem. Eng.* **14**, 253 (1998).
- ⁴Y. Kawaguchi, T. Segawa, Z. Feng, and P. Li, "Experimental study on drag-reducing channel flow with surfactant additives—spatial structure of turbulence investigated by PIV system," *Int. J. Heat Fluid Flow* **23**, 700 (2002).
- ⁵B. Yu, F. Li, and Y. Kawaguchi, "Numerical and experimental investigation of turbulent characteristics in a drag-reducing flow with surfactant additives," *Int. J. Heat Fluid Flow* **25**, 961 (2004).
- ⁶H.-W. Bewersdorff, in *Structure of Turbulence and Drag Reduction*, edited by A. Gyr (Springer, Berlin, 1990), pp. 293–312.
- ⁷Z. Chara, J. L. Zakin, M. Severa, and J. Myska, "Turbulence measurements of drag reducing surfactant systems," *Exp. Fluids* **16**, 36 (1993).
- ⁸G. Hetsroni, J. L. Zakin, and A. Mosyak, "Low-speed streak in drag-reduced turbulent flow," *Phys. Fluids* **9**, 2397 (1997).
- ⁹M. Itoh, S. Imao, and K. Sugiyama, "Characteristics of low-speed streaks in the flow of drag-reducing surfactant solution," *JSME Int. J., Ser. B* **40**, 550 (1997).
- ¹⁰M. D. Warholic, G. M. Schmidt, and T. J. Hanratty, "The influence of a drag-reducing surfactant on a turbulent velocity field," *J. Fluid Mech.* **388**, 1 (1999).
- ¹¹M. Nowak, "Time-dependent drag reduction and ageing in aqueous solutions of a cationic surfactant," *Exp. Fluids* **34**, 397 (2003).
- ¹²F.-C. Li, Y. Kawaguchi, T. Segawa, and K. Hishida, "Reynolds-number dependence of turbulence structures in a drag-reducing surfactant solution channel flow investigated by particle image velocimetry," *Phys. Fluids* **17**, 075104 (2005).
- ¹³F.-C. Li, Y. Kawaguchi, K. Hishida, and M. Oshima, "Investigation of turbulence structures in a drag-reduced turbulent channel flow with surfactant additive by stereoscopic particle image velocimetry," *Exp. Fluids* **40**, 218 (2006).
- ¹⁴F.-C. Li, Y. Kawaguchi, B. Yu, J.-J. Wei, and K. Hishida, "Experimental study of drag reduction mechanism for a dilute surfactant solution flow," *Int. J. Heat Mass Transfer* **51**, 835 (2008).
- ¹⁵J. E. Koskie and W. G. Tiederman, "Polymer drag reduction of a zero-pressure-gradient boundary layer," *Phys. Fluids A* **3**, 2471 (1991).
- ¹⁶J. E. Koskie and W. G. Tiederman, "Polymer drag reduction of a zero and adverse pressure gradient boundary layers," *Near-Wall Turbulent Flows*, edited by R. M. C. So, C. G. Speziale, and B. E. Laundaer (Elsevier, The Netherlands, 1993), pp. 659–668.
- ¹⁷A. A. Fontaine, H. L. Petrie, and T. A. Brungart, "Velocity profile statistics in a turbulent boundary layer with slot-injected polymer," *J. Fluid Mech.* **238**, 435 (1992).
- ¹⁸H. L. Petrie, S. Deutsch, T. A. Brungart, and A. A. Fontaine, "Polymer drag reduction with surface roughness in flat-plate turbulent boundary layer flow," *Exp. Fluids* **35**, 8 (2003).
- ¹⁹C. M. White, V. S. R. Somandepalli, and M. G. Mungal, "The turbulence structure of drag-reduced boundary layer flow," *Exp. Fluids* **36**, 62 (2004).
- ²⁰Y. Hou, V. S. R. Somandepalli, and M. G. Mungal, "A technique to determine total shear stress and polymer stress profiles in drag reduced boundary layer flows," *Exp. Fluids* **40**, 589 (2006).
- ²¹Y. Hou, V. S. R. Somandepalli, and M. G. Mungal, "Streamwise development of turbulent boundary-layer drag reduction with polymer injection," *J. Fluid Mech.* **597**, 31 (2008).
- ²²C. M. White and M. G. Mungal, "Mechanics and prediction of turbulent drag reduction with polymer additives," *Annu. Rev. Fluid Mech.* **40**, 235 (2008).
- ²³M. Itoh, S. Tamano, K. Yokota, and M. Ninagawa, "Velocity measurement in turbulent boundary layer of drag-reducing surfactant solution," *Phys. Fluids* **17**, 075107 (2005).
- ²⁴C. D. Dimitropoulos, Y. Dubief, E. S. G. Shaqfeh, P. Moin, and S. K. Lele, "Direct numerical simulation of polymer-induced drag reduction in turbulent boundary layer flow," *Phys. Fluids* **17**, 011705 (2005).
- ²⁵C. D. Dimitropoulos, Y. Dubief, E. S. G. Shaqfeh, and P. Moin, "Direct numerical simulation of polymer-induced drag reduction in turbulent boundary layer flow of inhomogeneous polymer solutions," *J. Fluid Mech.* **566**, 153 (2006).
- ²⁶S. Tamano, M. Itoh, K. Hoshizaki, and K. Yokota, "Direct numerical simulation on the drag-reducing turbulent boundary layer of viscoelastic fluid," *Phys. Fluids* **19**, 075106 (2007).
- ²⁷Y. T. Hu, P. Boltenhagen, and D. J. Pine, "Shear thickening in low-concentration solutions of wormlike micelles. I. Direct visualization of transient behavior and phase transitions," *J. Rheol.* **42**, 1185 (1998).
- ²⁸K. Gasljevic, K. Hoyer, and E. F. Matthys, "Temporary degradation and recovery of drag-reducing surfactant solutions," *J. Rheol.* **51**, 645 (2007).
- ²⁹D. E. Coles, "A manual of experimental boundary-layer practice for low-speed flow," RAND Report No. R-403-PR, 1962.
- ³⁰H. Schlichting, *Boundary-Layer Theory*, 7th ed. (McGraw-Hill, New York, 1979).
- ³¹V. M. Kulik, "Drag reduction change of polyethyleneoxide solutions in pipe flow," *Exp. Fluids* **31**, 558 (2001).
- ³²B. Yu and Y. Kawaguchi, "DNS of drag-reducing turbulent channel flow with coexisting Newtonian and non-Newtonian fluid," *J. Fluids Eng.* **127**, 929 (2005).
- ³³B. Lu, X. Li, L. E. Scriven, H. T. Davis, Y. Talmon, and J. L. Zakin, "Effect of chemical structure on viscoelasticity and extensional viscosity of drag-reducing cationic surfactant solutions," *Langmuir* **14**, 8 (1998).
- ³⁴C.-F. Li, R. Sureshkumar, and B. Khomami, "Influence of rheological parameters on polymer induced turbulent drag reduction," *J. Non-Newtonian Fluid Mech.* **140**, 23 (2006).
- ³⁵M. D. Warholic, H. Massah, and T. J. Hanratty, "Influence of drag-reducing polymers on turbulence: effects of Reynolds number, concentration and mixing," *Exp. Fluids* **27**, 461 (1999).
- ³⁶M. D. Warholic, D. K. Heist, M. Katcher, and T. J. Hanratty, "A study with particle-image velocimetry of the influence of drag-reducing polymers on the structure of turbulence," *Exp. Fluids* **31**, 474 (2001).
- ³⁷S. Baik, M. Vlachogiannis, and T. J. Hanratty, "Use of particle image velocimetry to study heterogeneous drag reduction," *Exp. Fluids* **39**, 637 (2005).
- ³⁸R. J. Adrian, "Hairpin vortex organization in wall turbulence," *Phys. Fluids* **19**, 041301 (2007).
- ³⁹S. K. Robinson, "Coherent motions in the turbulent boundary layer," *Annu. Rev. Fluid Mech.* **23**, 601 (1991).
- ⁴⁰K. Kim, C.-F. Li, R. Sureshkumar, S. Balachandar, and R. J. Adrian, "Effects of polymer stresses on eddy structures in drag-reduced turbulent channel flow," *J. Fluid Mech.* **584**, 281 (2007).
- ⁴¹K. Kim, R. J. Adrian, S. Balachandar, and R. Sureshkumar, "Dynamics of hairpin vortices and polymer-induced turbulent drag reduction," *Phys. Rev. Lett.* **100**, 134504 (2008).
- ⁴²H. W. Bewersdorff, J. Dohmann, L. Langowski, P. Lindner, A. Maack, R. Oberthür, and H. Thiel, "SANS- and LS-studies on drag-reducing surfactant solutions," *Physica B* **156–157**, 508 (1989).
- ⁴³B. Lu, X. Li, J. L. Zakin, and Y. Talmon, "A non-viscoelastic drag reducing cationic surfactant system," *J. Non-Newtonian Fluid Mech.* **71**, 59 (1997).
- ⁴⁴Z. Lin, Y. Zheng, H. T. Davis, L. E. Scriven, Y. Talmon, and J. L. Zakin, "Unusual effects of counterion to surfactant concentration ratio on viscoelasticity of a cationic surfactant drag reducer," *J. Non-Newtonian Fluid Mech.* **93**, 363 (2000).
- ⁴⁵P. A. Stone and M. D. Graham, "Polymer dynamics in a model of the turbulent buffer layer," *Phys. Fluids* **15**, 1247 (2003).
- ⁴⁶V. E. Terrapon, Y. Dubief, P. Moin, E. S. G. Shaqfeh, and S. K. Lele, "Simulated polymer stretch in a turbulent flow using Brownian dynamics," *J. Fluid Mech.* **504**, 61 (2004).